Corrosion maps: stability and composition diagrams for corrosion problems in CO_2 transport

Radomir I. Slavchov[*,1], Muhammad Hamza Iqbal[1,2], Saeid Faraji[1], David Madden[3], Johannes Sonke[4], Stuart M. Clarke[3]

[1]School of Engineering and Materials Science, Queen Mary University of London, Mile End Road, London E1 4NS, United Kingdom
[2]Department of Mechanical Engineering, University College London, London WC1E 7JE, UK
[3]Department of Chemistry and The Institute for Environment and Energy Flows, University of Cambridge, Lensfield Road, Cambridge, CB2 1EW
[4]Shell Global Solutions International B.V.
[*]e-mail: r.slavchov@qmul.ac.uk

Abstract. We present a Pourbaix-like graphical approach to assess the corrosive nature of impure CO_2 streams for carbon capture and storage purposes. The effects of critical N- and S-containing impurities is evaluated. The model behind the approach assumes that chemical equilibrium is established, with some kinetic effects accommodated. The input is the composition of the stream (total quantity of S, N, H and O) and the output is the equilibrium composition (speciation). Comparison with experimental data shows that the content of acids in the CO_2 stream upon reaching chemical equilibrium is a strong indicator of the corrosiveness of a given mixture.

Keywords: CO_2, purification, corrosion, carbon capture and storage, Pourbaix diagrams

List of symbols

C_E total concentration of the element E in all species present (C_S, C_N, C_H, C_C)
C_O excess concentration of oxygen (total oxygen in all species minus $2 \times C_C$, eq. (10))
f_p auxiliary quadrupolar factor in eq. (21)
G Gibbs energy
K equilibrium constant
k Boltzmann constant
$\lg X$ $\log_{10}(X)$
L_Q quadrupolar length
p pressure
p_0 molecular dipole moment in gaseous state
R_{cav} Onsager's cavity radius
T temperature
X_E elemental ratio, $X_E = C_E/C_S$ or $X_E = C_E/C_N$
X_p Onsager's reaction field factor
x the ratio $\underline{L_Q}/R_{cav}$
γ activity coefficient
$\Delta G^\ominus$ standard reaction Gibbs energy (standard state 1 mM)
μ chemical potential
α_p molecular polarizability
ε dielectric permittivity
ε_0 dielectric permittivity of vacuum

AHC NH_4HCO_3
CCS   Carbon Capture and Storage
ppm$x$ parts per million by mole

1 Introduction

To achieve net-zero emissions by 2050, humanity needs technologies for Carbon Capture and Storage (CCS). The International Energy Agency's analysis of the *announced pledges scenario* requires 350 Mt/y of captured CO_2 by 2030, whilst the *net zero emissions goals* require the colossal 2.5 Gt/y [1] – orders of magnitude more than existing capacities. CCS will be utilized initially to decarbonize large fossil fuel power plants; after those are phased out, CCS is expected to remain in extensive use for production of chemicals, synthetic fuels, steel, aluminium, and cement [2]. The projection of the Intergovernmental Panel on Climate Change [3] is that CCS must contribute an enormous 15-55% to the cumulative mitigation effort worldwide until 2100.

The widespread implementation of CCS requires it to be affordable. The main expenses are the cost of purification of CO_2 (currently ~80-95% of the total cost for the CO_2-producing plants [4]) and the investment cost for long-distance carbon steel pipelines [5-7], which currently make CCS a borderline break-even activity. A significant cost reduction can be achieved by relaxing the demanding impurity level specifications [2,4], a critical part of which originate from integrity and safety requirements related to corrosion [5-8]. Maximizing the load of impurities such as SO_x, NO_x, CO, H_2S in the CO_2 stream, without compromising safety and corrosion rates, is beneficial also from an environmental point of view [4].

No purity specifications for anthropogenic CO_2 transport have been universally accepted yet [9]. The opportunity is illustrated by the orders-of-magnitude difference in the impurity specifications in active CCS projects; e.g., the Weyburn-Midale EOR project in Canada allows H_2S levels as high as 9000 ppm$x$ (mole part per million) but requires nearly complete removal of water (20 ppm$x$), while the DYNAMIS project (EU's 6th Framework programme) allows for 500 ppm$x$ water but only 200 ppm H_2S. Specifications also vary greatly for NO_x, O_2 etc. [2,9] and depend on the approach used for carbon capture; see Table 1. Newer CCS projects have even more stringent specifications; for example, the Aramis pipeline requires $[H_2S] < 5$ ppm$x$, $[H_2S] + [SO_x] < 20$ ppm$x$, and $[H_2O] < 70$ ppm$x$ [10], close to the specifications for the Northern Lights project [11] and the values listed in the industrially accepted guidelines [7]. The most recent published work suggests $[H_2S] < 5$ ppm$x$, $[SO_x] < 10$ ppm$x$, $[H_2O] < 50$ ppm$x$ and $[NO_2] < 2.5$ ppm$x$ [8]. One reason for the increasingly demanding specifications is that recent CCS projects have CO_2 streams of different composition being mixed: CCS infrastructure that is currently being developed aims to capture CO_2 from a range of industrial emitters (the so-called hub or cluster CCS projects), where each emitter produces CO_2 streams of vastly dissimilar composition, whose mixing may trigger chemical reactions and new phase formation. This makes defining safe specifications a complex problem, involving many possible mixing schedules and chemical and physicochemical interactions of a wide combination of impurities [5,6,12]. A standardized corrosion test is urgently required for the purposes of CO_2 transport, but the vast number of mixing scenarios makes a practical design of such a test difficult to conceive [13]. Hence, it is vital to understand precisely what impurity concentrations in the CO_2 stream can be handled, how the different components interact and may separate out corrosive phases, what are the variants for the intermediate and final state of these mixtures etc.

3

Table 1. Typical impurity levels in the CO_2 streams from different source sites and specifications for CCS hubs.

Reduced streams (pre-combustion)		
H_2O	dew-point, 0.1–600 ppm$x$ [14]	
H_2S	< 3.4 vol% [15]	
	0.01–0.6 vol% [3]	
NH_3	38 ppm$x$ [14]	

Oxidized streams		
	Post-combustion	**Oxyfuel**
H_2O	100–640 ppm$x$ [14]	100–1000 ppm$x$ [14]
SO_x	< 10 ppm$x$ [14,16]	< 2.5 ppm$x$ [15,16]
NO_x	< 50 ppm$x$ [16]	< 0.25 ppm$x$ [15]
	20-38.8 ppm$x$ [14]	
O_2	< 0.01 %x [14,16]	< 3 %x [16]
		1.7 %x [15]

CCS hub projects (mixture of streams)		
	pipelines	**ship transport**
H_2O	50 ppm$x$ [8], 70 ppm$x$ [10]	30 ppm$x$ [10,11]
H_2S	5 ppm$x$ [8,10], 20 ppm$x$ [16]	5 ppm$x$ [10], 9 ppm$x$ [11]
SO_x	10 ppm$x$ [8], (20 ppm$x$ –[H_2S]) [10]	10 ppm$x$ [10,11]
NO_x	2.5 ppm$x$ [8, 10]	1.5 ppm$x$ [10,11]
O_2	10 ppm$x$ [8,16], 40 ppm$x$ [10]	10 ppm$x$ [10,11]
NH_3	3 ppm$x$ [10], 0-5 ppm$x$ [17]	10 ppm$x$ [11]

Integrity and safety risks linked to corrosion of the carbon steel pipelines have been directly related [5-8,12] to the phase separation of acids (H_2SO_4 and HNO_3, together with water and other polar admixtures). In relation to that, the stream purity specification depends on three main factors:

(i) the tendency of the mixture to produce H_2SO_4 and HNO_3. This is a chemical equilibrium composition problem for mixing streams from different CO_2 point sources that can react via oxidation-reduction and other reactions.

(ii) The equilibrium solubility of H_2SO_4 and HNO_3 (in the presence of water) in CO_2, within the operating window of pressure and temperature for the pipeline, and also under maintenance-related or accidental depressurization of the wider production system.

(iii) Kinetics. The factors (i-ii) set the equilibrium state of the stream, which is usually the worst-case scenario for corrosion that can be offset by altering the chemical or nucleation kinetics, for example with antioxidants, flow, or by targeting the formation of the new phase at bulk nuclei (e.g., hydrophilic particles) rather than on the pipe surface.

In this work, we will focus on the first question: we develop a set of diagrams and stability maps resembling the Pourbaix potential-pH diagrams in electrochemistry [18,19] and the Ellingham oxygen activity-temperature diagrams in high-temperature corrosion [18], to allow a quick prediction of the expected equilibrium chemical composition upon mixing streams and define some limits on the content of the CO_2 streams that will prevent corrosion due to drop-out of an acidic phase. The solubility and the kinetics (ii and iii above), including nucleation, will be investigated in subsequent studies, although some key questions will be raised and discussed here.

2 Theory

The typical impurity content of a CO_2 stream in the pipe includes a number of sulfur and nitrogen species of different oxidation state and hydration level; see Table 1. When two streams are mixed, or when conditions change (e.g., upon exposure to oxygen from the air), the impurities will react with each other via a series of oxidation-reduction and hydration-dehydration reactions until they equilibrate to a new composition, typically with only a few dominating species, of amounts corresponding to a specific activity of oxygen and water. For example, H_2S can be oxidized by O_2, NO_2 or SO_3 to produce elemental sulfur and SO_2; SO_3 can react with water to produce sulfuric acid. NO_x can similarly produce HNO_2 and HNO_3. The composition of the equilibrated stream can be predicted based on the thermochemical data for the gas phase, possibly also corrected for the effects arising from the presence of a solvent (dense CO_2) and nonideality due to molecular association. One can illustrate the composition for different conditions by using a variant of the approach of Pourbaix [18,19] to construct isothermal stability diagrams. This is discussed in sec. 2.1. The stability diagrams are easily converted to respective gas composition maps, investigated in sec. 2.2. The corrections for the solvent effect and the nonideality are considered in sec. 2.3-2.4 and will be included in the model as an extension in due course, but these appear to have little effect on the problem discussed here. The same two effects dramatically alter the solubility of the investigated species – a problem that will be discussed in a separate study.

2.1   Stability maps for gas phase

Sulfur. The following schematic lists the sulfur species that can be expected at chemical equilibrium in the carbon dioxide phase, according to their oxidation state and hydrogen content (H_n indicates the number of hydrogen atoms in the molecule):

2+	0	4-	6-	
	S $\longrightarrow$	$SO_2 \longrightarrow$	SO_3	(**H$_0$**)
H_2S			H_2SO_4	(**H$_2$**)

Other sulfur species, like SO and H_2SO_3, were found to be thermodynamically unstable in the gas phase and tend to convert to the five compounds in the table.

The state of the mixture after equilibration depends on the overall elemental ratios S:O:H (considering the total of all species present in the mixture). The compositional dependence can be illustrated on a diagram showing the sulfur species present at highest concentration under equilibrium conditions as a function of the oxidation and hydration potentials of the mixture, as measured by the activity of oxygen and water, respectively. Such a diagram is similar to both the potential vs pH and $\log p_i$-$\log p_j$ isothermal stability diagrams of Pourbaix [18,19].

Consider, as a first example, the equilibrium between SO_2 and SO_3 ($SO_2 + \frac{1}{2}O_2 \rightleftarrows SO_3$). Assume that SO_2 and SO_3 are the dominating sulfur compounds in the mixture and all other sulfur species are of negligible concentration. Let the total concentration of sulfur in all species present be C_S. At the *equistability line*, the two species are of equal concentration:

$[SO_2] = [SO_3] = C_S/2$. Then, the equilibrium condition, $[SO_3]/[SO_2][O_2]^{1/2} = K_{SO2/SO3}$, predicts that the activity of O_2 on the equistability line is constant:

$$lgO_2 = -2lgK_{SO2/SO3}. \tag{1}$$

Here, lgO_2 denotes $log_{10}[O_2]$; we have assumed ideal behaviour. In coordinates lgO_2 vs lgH_2O, eq. (1) corresponds to a horizontal line separating the region where the mixture is dominated by SO_2 from the region of SO_3 (Figure 1). As a first approximation, for $K_{SO2/SO3}$ we can use the gas-phase value, calculated through Hess's law and Van 't Hoff's or Kirchhoff's equation from gas thermodynamic data [21-23] at the temperature of interest. We have converted the K values for standard state of 1 bar (as usual for gases) to mM-based. This is because concentration is preferrable to partial pressure or mole fraction for the study of the effects of the solvent, of the pressure of the liquid CO_2 and of any dimerization of solute species on their solubilities in CO_2. For convenience, the conversion rules are listed in S1 in the supplementary information.

As a second example, consider the gas-phase equilibrium $SO_2 + H_2O + \frac{1}{2}O_2 \rightleftarrows H_2SO_4$, which specifies the boundary between the SO_2- and H_2SO_4-dominated regions. The equilibrium condition ($[H_2SO_4]/[SO_2][H_2O][O_2]^{1/2} = K_{SO2/H2SO4}$) where SO_2 and CO_2-dissolved H_2SO_4 are equally stable (i.e. where $[SO_2] = [H_2SO_4]$) can be written as:

$$lgO_2 = -2lgK_{SO2/H2SO4} - 2lgH_2O. \tag{2}$$

This is correct under the assumption that H_2SO_4 does not precipitate as a new phase (for example, when it is below its solubility limit or due to hindered kinetics of the new phase formation). This is indeed the case we care about: the conditions in the pipeline should preclude the formation of a polar acidic phase. Thus, the line of equal stability (2) is of slope −2 in the stability diagram plotted in coordinates lgO_2 vs lgH_2O (Figure 1).

For reactions involving solid sulfur, S(s), the total amount of sulfur is distributed between two different phases, CO_2 solution and solid. For example, consider the oxidation of sulfur:

$$S(s) + O_2(g) \rightleftarrows SO_2(g), \qquad and [SO_2]/[O_2] = K_{S/SO2};$$

the activity of S(s) is 1. In this case, as long as any solid sulfur is present, the concentration of SO_2 is given by $K_{S/SO2} \times [O_2]$; if $K_{S/SO2} \times [O_2]$ is larger than the total C_S, the solid sulfur will disappear completely. For two phases, we can still define the line of equal stability of S and SO_2 as the point where $[SO_2]$ reaches $\frac{1}{2}C_S$ (half the total amount of sulfur present). This leads to:

$$lgO_2 = -lgK_{S/SO2} + lg(\frac{1}{2}C_S), \tag{3}$$

which is another horizontal line in Figure 1. Unlike the previous two equistability conditions (1)&(2), this one depends on the total concentration of sulfur, C_S. Fortunately, this is a weak logarithmic dependence and for the relevant range, C_S = 1-100 mM, C_S has only a small effect on the stability map (see Figure 1), and this effect has no consequences at all when mass distribution diagrams are considered (see sec. 2.2 below). High levels of total sulfur tend to expand the region where solid sulfur is the dominating compound.

Thus, combining all equistability lines (listed in Table 2), we construct a complete Pourbaix-like stability diagram. Instead of redox potential (as in the original Pourbaix diagram [19]), oxygen activity, $log_{10}([O_2]/mM)$, is used on the abscissa; the value of the oxygen activity, like the redox potential of a metal, is a direct measure of the oxidation activity in the system (Pourbaix himself often uses $RTlnp_{O2}$ as a second axis parallel to the potential axis [18]). For high values of lgO_2, the oxygen activity is equal to the oxygen concentration $[O_2]$ in the mixture. A value of $[O_2]$ of 10^{-60} mM, however, is physically meaningless and should be treated as a measure of the oxidation potential of the oxygen-containing species present in the mixture.

This is similar to the way oxygen activity is treated when the oxide layers on a metal are studied [20].

Based on the diagram in Figure 1, it turns out that it is impossible for some couples of sulfur species to coexist after equilibration: for example, H_2S and SO_2 cannot both be present in the mixture at equilibrium (as claimed in, e.g., ref. [8]) since they react irreversibly to produce sulfur. Moreover, neither SO nor H_2SO_3 are stable in the considered temperature range (they are prone to irreversible decomposition in the gaseous/CO_2 phase: $H_2SO_3 \rightarrow SO_2 + H_2O$, and $2SO \rightarrow SO_2 + S$). On the other hand, since CO_2 is present in the stream, a mixed species containing both C and S appears in Figure 1: COS, as explained below.

Table 2. Equistability boundaries for the stability diagram of sulfur compounds.

short	full reaction	equistability line
H_2S/S	$H_2S + \frac{1}{2}O_2 \rightleftarrows S + H_2O$	$\lg O_2 = -2\lg K_{H_2S/S} - 2\lg(\frac{1}{2}C_S) + 2\lg H_2O$
S/SO_2	$S + O_2 \rightleftarrows SO_2$	$\lg O_2 = -\lg K_{S/SO_2} + \lg(\frac{1}{2}C_S)$
SO_2/SO_3	$SO_2 + \frac{1}{2}O_2 \rightleftarrows SO_3$	$\lg O_2 = -2\lg K_{SO_2/SO_3}$
H_2S/H_2SO_4	$H_2S + 2O_2 \rightleftarrows H_2SO_4$	$\lg O_2 = -\frac{1}{2}\lg K_{H_2S/H_2SO_4}$
S/H_2SO_4	$S + H_2O + \frac{3}{2}O_2 \rightleftarrows H_2SO_4$	$\lg O_2 = -\frac{2}{3}\lg K_{S/H_2SO_4} + \frac{2}{3}\lg(\frac{1}{2}C_S) - \frac{2}{3}\lg H_2O$
SO_2/H_2SO_4	$SO_2 + H_2O + \frac{1}{2}O_2 \rightleftarrows H_2SO_4$	$\lg O_2 = -2\lg K_{SO_2/H_2SO_4} - 2\lg H_2O$
SO_3/H_2SO_4	$SO_3 + H_2O \rightleftarrows H_2SO_4$	$\lg H_2O = -\lg K_{SO_3/H_2SO_4}$ (a vertical line)

All equilibrium constants refer to standard state of 1 mM (converted from 1 bar as in CRC [21]); the actual room-temperature values are listed in S1 in the supplement.
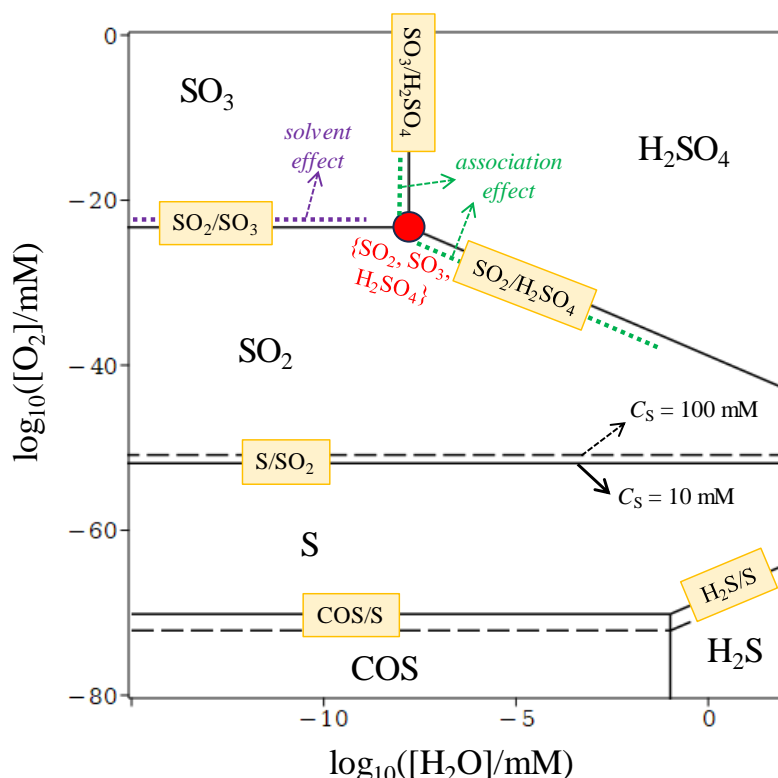

Figure 1. Stability diagram of sulfur compounds vs activity of oxygen and water (25 °C). Each line on this diagram corresponds to an equation in Table 2, as indicated in the rectangles. The solvent effect (sec. 2.3), the nonideality effect (sec. 2.4), and the effect from the total concentration of sulfur are illustrated.

The diagram in Figure 1 assumes that the reactions of the impurities proceed to the equilibrium composition. However, there are particular issues around the formation and subsequent reaction of solid sulfur. The formation of solid sulfur can involve a slow rate-limiting nucleation stage; moreover, the subsequent reactions of S may well be dramatically decelerated by the diffusion kinetic control typical for reactions involving solids. Hence, it is noted that formation or disappearance of solid sulfur may act as a kinetic block, as supported by experimental data (see sec. 3 below).

Nitrogen. The most stable nitrogen species under pipeline conditions is N_2. However, the available data [6,8,24] suggest that it does not form under these conditions, at least not in significant amount, due to the energy barrier for formation of the triple $N{\equiv}N$ bond. Another relatively stable species, N_2O, is difficult to form for the same reason. Indeed, reactions proceeding with formation of multiple NN bonds are untypical at room temperature [24], in the absence of a catalyst. Therefore, we assume a kinetically arrested composition where none of the nitrogen impurities in the initial mixture converts to N_2 or N_2O. Of course, any N_2 initially present remains, but this should not be added to the total concentration of 'reactive' nitrogen species, C_N.

The reactive nitrogen species considered here are the following:

3+	2-	3-	4-	5-
	NO $\longrightarrow$		NO$_2$	(**H$_0$**)
		HNO$_2$		HNO$_3$	(**H$_1$**)
NH$_3$					(**H$_3$**)
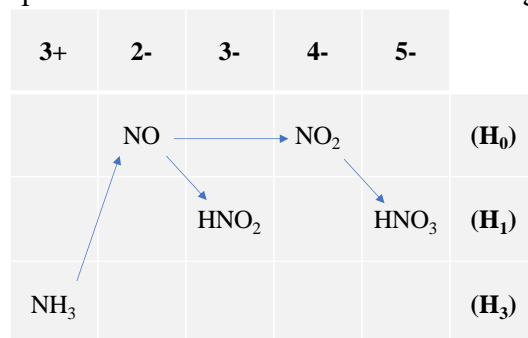
The composition is again controlled by the activity of oxygen and water, as illustrated in the stability diagram of these nitrogen species in Figure 2. The reactions and the equations for the equistability lines are listed in Table 3, and the respective values of the equilibrium constants are given in S1. CRC [21] cite a rather different formation energy for gaseous HNO_2 compared to NIST [22]; below, we use the CRC value as it corresponds to the worst-case scenario (more acid).

Table 3. Region boundaries for the stability diagram of nitrogen compounds.

short	full reaction	equal stability
NH$_3$/NO	$NH_3 + {}^5\!/_4 O_2 \rightleftharpoons NO + {}^3\!/_2 H_2O$	$\lg O_2 = -{}^4\!/_5 \lg K_{NH3/NO} + {}^6\!/_5 \lg H_2O$
NO/NO$_2$	$NO + {}^1\!/_2 O_2 \rightleftharpoons NO_2$	$\lg O_2 = -2\lg K_{NO/NO2}$
HNO$_2$/HNO$_3$	$HNO_2 + {}^1\!/_2 O_2 \rightleftharpoons HNO_3$	$\lg O_2 = -\lg K_{HNO2/HNO3}$
NO/HNO$_2$	$NO + {}^1\!/_2 H_2O + {}^1\!/_4 O_2 \rightleftharpoons HNO_2$	$\lg O_2 = -4\lg K_{NO/HNO2} - 2\lg H_2O$
NO$_2$/HNO$_2$	$NO_2 + {}^1\!/_2 H_2O \rightleftharpoons HNO_2 + {}^1\!/_4 O_2$	$\lg O_2 = 4\lg K_{NO/HNO2} + 2\lg H_2O$
NO$_2$/HNO$_3$	$NO_2 + {}^1\!/_2 H_2O + {}^1\!/_4 O_2 \rightleftharpoons HNO_3$	$\lg O_2 = -4\lg K_{NO2/HNO3} - 2\lg H_2O$

All equilibrium constants refer to standard state 1 mM (rather than 1 bar as in CRC [21]). The actual room-temperature values are listed in S1.

Nitrogen's stability diagram is read in a similar manner to the one for sulfur above. For example, according to Figure 2, NO_2 and HNO_2 can coexist in significant concentrations (under

conditions close to those along the NO_2/HNO_2 line); by contrast, NO and HNO_3 will react irreversibly to form more stable HNO_2 or NO_2.
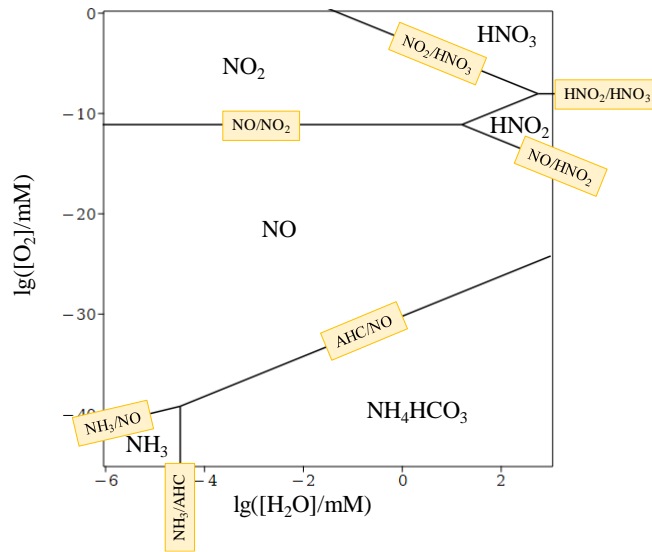

Figure 2. Stability diagram of nitrogen compounds vs activity of oxygen and water (25 °C). Each line on this diagram corresponds to an equation in Table 3. The NH_4HCO_3 region is shown for $C_N = 5$ mM.

Most likely, the conversion from NH_3 to NO is also kinetically arrested. Ammonia does not normally react with O_2 at room temperature [24], and NO is similarly difficult to reduce. However, radicals present in the mixed stream (e.g., NO_2) may initiate an oxidation process under special circumstances. For example, in the absence of water and in the presence of NO and NO_2, the following mechanism may allow the oxidation of ammonia and the reduction of NO through the amino radical $NH_2\cdot$ [25-27]:

$$NH_3 + NO_2 \rightarrow NH_2\cdot + HNO_2;$$
$$NH_2\cdot + NO \rightarrow NH_2NO \rightarrow \ldots \rightarrow N_2, N_2O. \qquad (4)$$
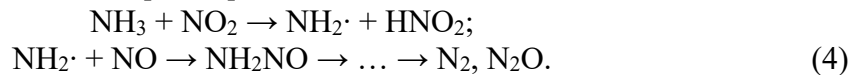
However, we will assume that oxidation of NH_3 and reduction of NO is not taking place, again as a worst-case scenario for the mixtures considered below (which do not contain NH_3).

Ammonia present is nevertheless important, as it may form various salts with the acids and acidic oxides in the stream. If only nitrogen species are present, then HNO_2 or HNO_3 may form salts with NH_3 [24]:

$$NH_3 + HNO_x \rightarrow NH_4NO_x(s)\downarrow. \qquad (5)$$
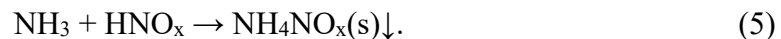
This process takes place even though the electrolytes NH_4NO_x are thermodynamically less stable than NH_3 and NO (e.g., the reaction $5NH_4NO_3 \rightarrow 2NH_3 + 8NO + 7H_2O$ is in theory irreversible), due to the slow oxidation kinetics of NH_3 (or NH_4^+). In the presence of CO_2 and water, ammonium carbonates can be expected as explained below. Salts with H_2S and H_2SO_4 are also possible.

Carbon. In a CO_2 medium, one should consider the equilibrium:

$$CO + \frac{1}{2}O_2 \rightleftarrows CO_2.$$
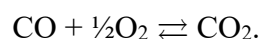
The two oxides are equally stable when $[CO] = [CO_2]$ and $lgO_2 = -2lgK_{CO/CO2}$. More relevant, however, is the point where the amount of CO becomes comparable with C_S and C_N. If $[CO] = C_S + C_N$ is chosen as the boundary line, and expecting that $[CO] << [CO_2] \approx C_C$, then the respective boundary in the stability diagram is:

$$lgO_2 = -2lgK_{CO/CO2} - 2lg[(C_S + C_N)/C_C]. \qquad (6)$$

9

The typical amounts of impurities in the CO_2 stream are mole fractions in the range $(C_S+C_N)/C_C = 5...1000$ ppm$x$, which corresponds to a horizontal CO/CO_2 line at $lgO_2 = -77.9...-82.5$; that is, when the oxidation potential of the mixture corresponds to $lgO_2 = -77.9$, carbon monoxide will be produced from the reduction of CO_2, of mole fraction 5 ppm$x$. The activity coefficient of CO_2 can be taken into account; we compared several Aspen methods [23] to find it is of the order of 0.5-0.6, shifting the lgO_2 line (6) down by 0.5-0.6 units.

Combined stability diagrams. The lgO_2 vs lgH_2O diagrams of S, N, and C can be combined directly, unless mixed species (like $(NH_4)_2CO_3$, COS, NH_4HS, urea, formamide…) appear; that is, the boundary lines defined in Table 2 and Table 3 remain the same for the mixture of elements. However, several mixed C,S,N species are actually thermodynamically stable in excess of CO_2 at low lgO_2. The first one is COS, which appears between S and H_2S among the sulfur compounds in Figure 1. The horizontal line between the S and COS regions in Figure 1 stands for the equilibrium:

$$COS + \tfrac{1}{2}O_2 \rightleftarrows CO_2 + S(s), \qquad [CO_2]/[COS][O_2]^{1/2} = K_{COS/S}.$$

This leads to the following equistability condition for COS and S:

$$lgO_2 = -2lgK_{COS/S} - 2lg(C_S/C_C). \qquad (7)$$

The other relevant boundary, COS/H_2S, is given in Table 4 and Figure 1 (for $C_C = 18.55$ M, corresponding to 100 bar and 25 °C).

On the other hand, NH_3 forms carbonates with CO_2:

$$NH_3 + CO_2 + H_2O \rightleftarrows NH_4HCO_3(s), \qquad 1/[NH_3][CO_2][H_2O] = K_{NH3/AHC}.$$

The zone where NH_4HCO_3 can be expected is illustrated in Figure 2; the equations of the respective boundaries are given in Table 4. Compared to NH_4HCO_3, other mixed species like urea and carbamic acid are less stable; however, in case that the formation of the solid NH_4HCO_3 is kinetically hindered, dissolved $(NH_2)_2CO$ may form instead (at $lgH_2O > -2.9$ and $lgO_2 < -35.0 + \tfrac{4}{5}lgH_2O$) and eventually precipitate as solid urea.

Another important class of species is the solid products of the neutralization reaction between H_2S and NH_3 – various solid ammonium hydrogen sulfides:

$$xNH_3 + H_2S \rightarrow (NH_4)_xH_{2-x}S(s).$$
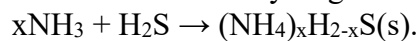
Similarly, if NH_3 is present and its oxidation is arrested, ammonium sulfate may appear at higher lgO_2.

Table 4. Region boundaries for the combined S,N stability diagram.

short	full reaction	equal stability
COS/H_2S	$COS + H_2O \rightleftarrows CO_2 + H_2S$	$lgH_2O = -lgK_{COS/H2S} + lgC_C$
COS/S	$COS + \tfrac{1}{2}O_2 \rightleftarrows CO_2 + S$	$lgO_2 = -2lgK_{COS/S} - 2lg(C_S/C_C)$
NH_3/AHC	$NH_3+CO_2+H_2O \rightleftarrows NH_4HCO_3(s)$	$lgH_2O = -lgK_{NH3/AHC} - lg(\tfrac{1}{2}C_N) - lgC_C$
AHC/NO	$NH_4HCO_3(s) + \tfrac{5}{4}O_2 \rightleftarrows$ $NO + \tfrac{5}{2}H_2O + CO_2$	$lgO_2 = -\tfrac{4}{5} \times lgK_{AHC/NO}$ $+ \tfrac{4}{5}lg(\tfrac{1}{2}C_N) + 2lgH_2O + \tfrac{4}{5}lgC_C$

All equilibrium constants refer to standard state 1 mM (rather than 1 bar as in CRC [21]). The actual room-temperature values are listed in S1.

The combined diagram is plotted in Figure 3, in two variants: one with NH_3 derivatives and a second where it is assumed that, for kinetic reasons, no nitrogen species more reduced than NO can appear. Only the second stability map is relevant to the data which we investigate in sec. 3, where no NH_3 is present initially or is expected to form during the experiment. However, for streams containing NH_3 initially, its chemistry should be considered as well.

Moreover, the CO_2 streams often contain ethanolamine and alkylamines from scrubbing, which also come with chemistry of their own (precipitation, acid-base and radical chain reactions). In addition, CO will appear in Figure 3 below $lgO_2 \approx -80$, but such conditions are also irrelevant to the considered experimental data – the equistability line between CO and CO_2 is well outside the range where the corrosive acids H_2SO_4 and HNO_3 appear. Hence, for the conditions of interest for CCS, CO_2 is considered to remain intact.

According to Figure 3, SO_2, SO_3, and NO can coexist but SO_2 and NO_2 cannot (because NO_2 will oxidize SO_2 in an irreversible reaction). Similarly, H_2SO_4, NO_2 and SO_3 can coexist, but HNO_3 and SO_3 cannot (as HNO_3 will hydrate SO_3).
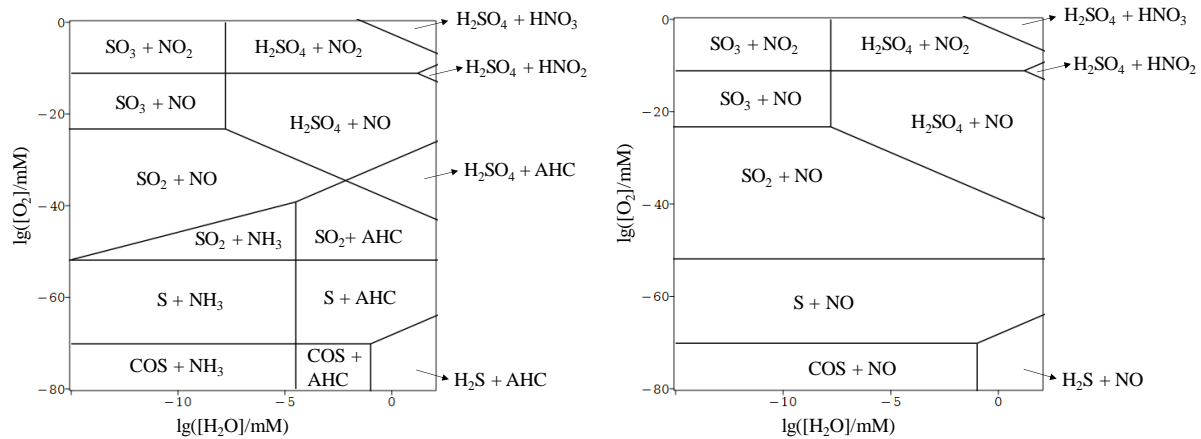

Figure 3. Combined stability diagrams. AHC stands for NH_4HCO_3. The right variant assumes that the formation of NH_3 is kinetically arrested (along with N_2 and N_2O).

2.2   Maps of the dominating components

When several CO_2 streams of different impurity content are mixed, the total concentrations of H, S and N are related to the concentration of species (before or after reaction) as:

$$C_H = 2[H_2O] + 2[H_2S] + [HNO_x] + 2[H_2SO_4];$$
$$C_S = [COS] + [S] + [H_2S] + [SO_x] + [H_2SO_4];$$
$$C_N = [NO_x] + [HNO_x]. \tag{8}$$

The total concentration of nitrogen does not involve the molecular nitrogen, ammonia and ammonium salts, as explained above. To avoid working with large numbers, for the mass balance of oxygen, the excess oxygen element in excess of the carbon present is used, defined as:

$$C_O = 2[O_2] + [H_2O] + x[NO_x] + x[SO_x] + x[HNO_x] + 4[H_2SO_4] - [CO] - [COS]. \tag{9}$$

Here, 'excess' means that CO is so normalized that pure CO_2 (of the same total carbon amount) would have no excess oxygen, namely:

$$C_O = C_{O,tot} - 2C_C = C_{O,tot} - 2\times([CO] + [CO_2] + [COS]). \tag{10}$$

CO and COS have one oxygen less than CO_2, which is why they appear with stoichiometric coefficient -1 in eq. (9). Thus, the excess C_O can be negative in a reduced stream of high CO + COS content.

Case of sulfur only – dominating component vs element ratios. The stability map in Figure 1 tells us that normally only a few species are present in the mixture in significant concentration after equilibration, even for complex initial composition. For example, in excess of oxygen and water, all sulfur will be converted to H_2SO_4 and only three species will be present in the mixture in significant concentrations: H_2SO_4, O_2 and H_2O. In this case, the mass balances (8)-(9) after equilibration simplify to:

11

$$C_O = 2[O_2] + [H_2O] + 4[H_2SO_4];$$
$$C_H = 2[H_2O] + 2[H_2SO_4];$$
$$C_S = [H_2SO_4]. \tag{11}$$

These equations can be solved for the species concentrations to give:

$$[O_2] = \tfrac{1}{2}C_O - \tfrac{1}{4}C_H + \tfrac{3}{2}C_S;$$
$$[H_2O] = \tfrac{1}{2}C_H - C_S;$$
$$[H_2SO_4] = C_S. \tag{12}$$

These concentrations must be positive, i.e. the conditions $[O_2] > 0$ and $[H_2O] > 0$ have to be fulfilled. These inequalities lead to the following boundaries of the $\{H_2SO_4, O_2, H_2O\}$ region:

$$X_O > \tfrac{1}{2}X_H + 3; \qquad X_H > 2. \tag{13}$$

Here, two elemental ratios appear: $X_H = C_H/C_S$ is the ratio of hydrogen to sulfur, and $X_O = C_O/C_S$ is the ratio of excess oxygen to sulfur. The region is illustrated in Figure 4-left, in the coordinate system X_O vs X_H.

We can find the coexistence region boundaries for each possible 3-species mixture in a similar manner, as well as a respective formula for the concentration of H_2SO_4. The boundaries and the expressions for $[H_2SO_4]$ are listed in Table 5, and the regions are illustrated in Figure 4. Importantly, in the regions where H_2SO_4 is a major component, the values of the equilibrium constants do not affect the value of this acid's concentration; $[H_2SO_4]$ is entirely determined by the mass balances of S, H and O.

Table 5. Boundaries of the 3-species regions and respective concentrations of H_2SO_4.

dominating species	boundaries	$[H_2SO_4]$
$\{H_2SO_4, H_2O, O_2\}$	$X_H = 2;\ X_O = 3 + \tfrac{1}{2}X_H$	C_S
$\{H_2SO_4, SO_3, O_2\}$	$X_H = 2;\ X_O = 3 + \tfrac{1}{2}X_H$	$\tfrac{1}{2}C_H$
$\{H_2SO_4, SO_3, SO_2\}$	$X_O = 3 + \tfrac{1}{2}X_H$ $X_O = 2 + X_H$	$\tfrac{1}{2}C_H$
$\{H_2SO_4, SO_2, H_2O\}$	$X_O = 3 + \tfrac{1}{2}X_H$ $X_O = 2 + \tfrac{1}{2}X_H$ $X_O = 2 + X_H$	$C_O - 2C_S - \tfrac{1}{2}C_H$
$\{SO_2, S, H_2O\}$	$X_O = 2 + \tfrac{1}{2}X_H$ $X_O = \tfrac{1}{2}X_H$	a small fraction of C_S: $[H_2SO_4] = K\,[SO_2]^{3/2}[H_2O]$, where $[SO_2] \approx \tfrac{1}{2}C_O - \tfrac{1}{4}C_H,\ [H_2O] \approx \tfrac{1}{2}C_H,$ $K \equiv (K_{SO2/H2SO4})^{3/2}(K_{S/H2SO4})^{-1/2}$
$\{S, H_2S, H_2O\}$	$X_O = \tfrac{1}{2}X_H$ $X_O = -2 + \tfrac{1}{2}X_H$	negligible
$\{S, COS, H_2S\}$	$X_O = -1 + \tfrac{1}{2}X_H$ $X_O = 0$ (where $X_O < 0$)	negligible

Each region in the 3-species diagram in Figure 4 corresponds to a single point on the stability map (Figure 1) at the boundary between three stability regions – for example, the point between SO_2, SO_3 and H_2SO_4 (the red point in Figure 1) is mapped in the centroid of the $\{H_2SO_4, SO_3, SO_2\}$ triangle in Figure 4. The equistability lines in Figure 1 are mapped as medians of the respective regions in Figure 4. The whole $\{SO_2, SO_3, H_2SO_4\}$ triangle in Figure 4 can be shown to map back to the immediate vicinity of the $\{SO_2, SO_3, H_2SO_4\}$ point in Figure 1.

The lines in Figure 4 correspond to conditions where two species dominate the mixture. For example, the boundaries (13) correspond to H_2SO_4 and O_2 (on $X_H = 2$), and H_2SO_4 and H_2O

(on $X_O = \frac{1}{2} X_H + 3$). These features are of interest for two reasons. The first is that when the composition is near, e.g., the $SO_2 + H_2O$ line in Figure 4, the mixture will be less corrosive than both more oxidized and less oxidized compositions, as both H_2S and H_2SO_4 are more dangerous than SO_2 alone. The second is that the composition nearby a line is more sensitive to temperature and solvent effects. The formulae (12) are an approximation of the full balances (8) that works best far away from the boundaries of the $\{H_2SO_4, O_2, H_2O\}$ region. For example, nearby $X_H = 2$, some SO_3 will appear, of concentration controlled by the equilibrium reaction that produces it:

$$[SO_3] = [H_2SO_4]/(K_{SO_3/H_2SO_4} \times [H_2O]) \approx 2/[K_{SO_3/H_2SO_4} \times (X_H - 2)]. \qquad (14)$$

This concentration increases as the boundary $X_H = 2$ is approached. SO_2 will similarly appear nearby $X_O = \frac{1}{2}X_H + 3$ etc. This is particularly important when the appearing species is H_2SO_4: some amount of the acid will be present below the $SO_2 + H_2O$ line, see Table 5, and this amount depends on a respective equilibrium constant which is temperature and pressure dependent.

It can be shown that the transition from one region to another is sharper (i.e. the conditions at the lines are closer to only two species present) when the regions in the respective stability diagram (Figure 1) are more widely spaced.
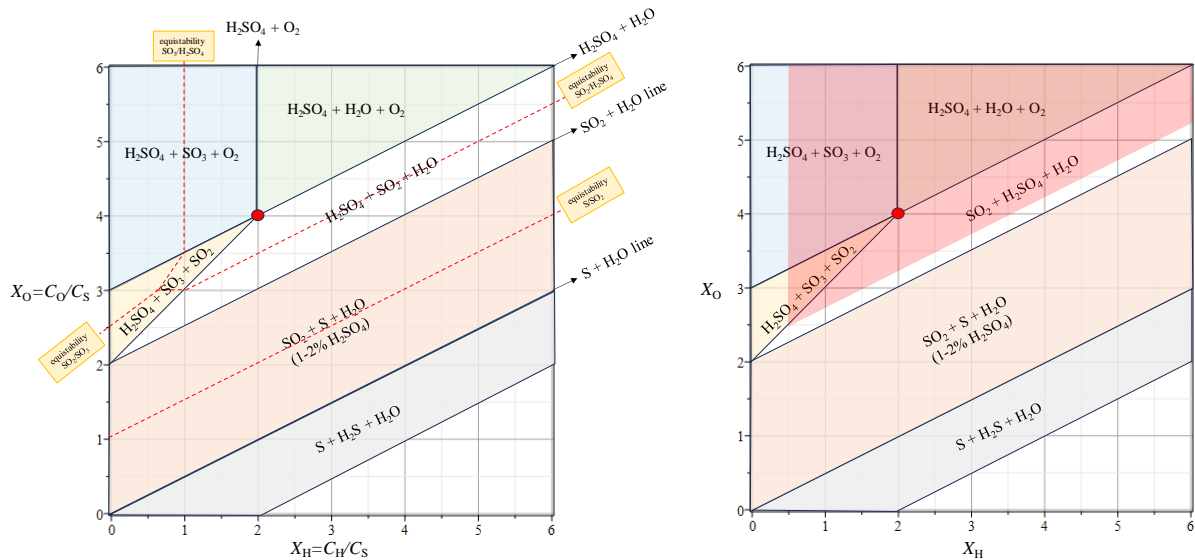

Figure 4. Left: 3-species diagram of sulfur species (mass-balance map). The red point corresponds to the stoichiometry of H_2SO_4 ($X_H = 2$, $X_O = 4$). Right: the triangular corrosion/phase separation region on the diagram indicates where $[H_2SO_4] > [H_2SO_4]_{cr}$.

The formulae for $[H_2SO_4]$ in Table 5 allow us to define the region where phase separation of $[H_2SO_4]$ takes place. The data from ref. [8] suggest that such phase separation occurs at concentration of H_2SO_4 above a certain critical $[H_2SO_4]_{cr} \approx 0.5$ mM (see sec. 3 below). The region where $[H_2SO_4] > [H_2SO_4]_{cr} \approx 0.5$ mM appears as a triangular area on the 3-species diagram, as shown in Figure 4-right. The limits, however, will shift with the total concentration of sulfur-containing species (expanding towards the y-axis and the SO_2 line as C_S increases).

Based on these results, corrosion can be avoided if the stream is (i) kept reduced (X_O below the SO_2 line in Figure 4); (ii) all H_2S and H_2O is removed during the separations stage (i.e. keeping X_H close to zero, but this is probably unfeasible); (iii) the total sulfur is kept low (if $C_S < [H_2SO_4]_{cr}$, no corrosion will take place, even if all available sulfur converts to H_2SO_4).

Case of nitrogen only. The same procedure is used to construct the 3-species diagram for the nitrogen compounds in Figure 2. As explained above, we ignore the presence of N-species

more reduced than NO, as these are expected to be kinetically arrested. The region boundaries are listed in Table 6 and the diagram is plotted in Figure 5. As with the sulfur map, there exists a NO_2 line (indicated with an arrow in Figure 5) where all the available nitrogen is expected to remain in the form of NO_2, without formation of HNO_2 or HNO_3.

Table 6. Boundaries of the 3-species regions for N and respective concentrations of HNO_x.

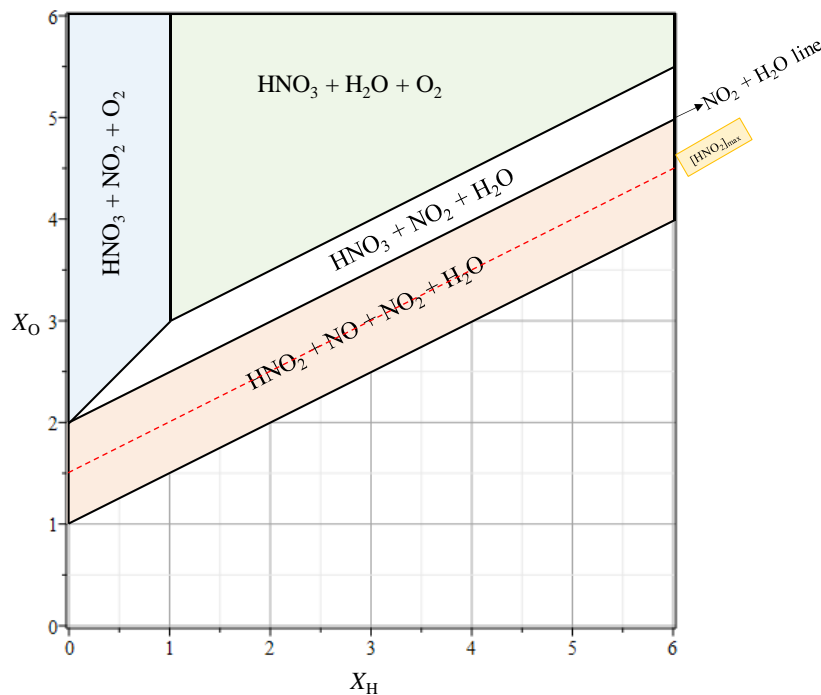| dominating species	boundaries	[HNO₃] + [HNO₂]
$\{HNO_3, H_2O, O_2\}$	$X_H = 1$ $X_O = {}^5\!/_2 + \tfrac{1}{2}X_H$	C_N
$\{HNO_3, NO_2, O_2\}$	$X_H = 1$ $X_O = 2 + X_H$	C_H
$\{HNO_3, NO_2, H_2O\}$	$X_O = {}^5\!/_2 + \tfrac{1}{2}X_H$ $X_O = 2 + X_H$ $X_O = 2 + \tfrac{1}{2}X_H$	$2C_O - C_H - 4C_N$
$\{HNO_2, NO, NO_2, H_2O\}$	$X_O = 2 + \tfrac{1}{2}X_H$ $X_O = 1 + \tfrac{1}{2}X_H$	solution to eq. (16)

Figure 5. 3-species diagram of nitrogen species.

The only general new feature that appears in the 3-species diagram of nitrogen compared to sulfur is a region where four species coexist: HNO_2, NO, NO_2 and H_2O. This is because the equilibrium

$$2HNO_2 \rightleftarrows NO + NO_2 + H_2O \qquad (15)$$

has an equilibrium constant of $K_{HNO2/NO/NO2} = 16$ mM at room temperature, which corresponds to a partial equilibrium conversion (all other considered reactions are approximately irreversible except on the boundary lines). In such cases, several 3-species regions merge into one (i.e. rather than having three separate 3-species regions $\{HNO_2, NO_2, NO\}$, $\{HNO_2, NO_2, H_2O\}$,

and {HNO_2, NO, H_2O}, there appears a single merged 4-species region). This feature of the system can be noticed already on the stability diagram in Figure 2, where the point between the HNO_2, NO, and NO_2 regions appears at lgH_2O in the mM range. More generally, similar situations will be also the case when two points between regions appear close to each other in the stability map (less than one unit difference), or when a point appears at lgO_2 in the mM range (in which case, one of the four components will be oxygen).

In this 4-species region of the nitrogen diagram, the prediction of the composition requires an equilibrium condition; i.e. the composition ([H_2O], [HNO_2], [NO] and [NO_2]) is determined by four equations – three mass balances and one condition for equilibrium:

$$C_O = [H_2O] + 2[HNO_2] + [NO] + 2[NO_2];$$
$$C_H = 2[H_2O] + [HNO_2];$$
$$C_N = [HNO_2] + [NO] + [NO_2];$$
$$[NO][NO_2][H_2O]/[HNO_2]^2 = K_{HNO2/NO/NO2}. \tag{16}$$

This system of equations results in a cubic equation for [HNO_2]. One can show that the maximum concentration of HNO_2 as a function of C_O appears at $C_O = \frac{3}{2} \times C_N + \frac{1}{2} \times C_H$, which is right in the middle of the {HNO_2, NO, NO_2, H_2O} region as illustrated in Figure 5. The respective maximum concentration of acid is the solution to:

$$\left(C_N - [HNO_2]_{max}\right)^2 \left(C_H - [HNO_2]_{max}\right) = 8K_{HNO_2/NO/NO_2}[HNO_2]_{max}^2 .$$

This is conveniently solved for C_H vs [HNO_2]$_{max}$:

$$C_H = [HNO_2]_{max} + 8K_{HNO_2/NO/NO_2}\left(\frac{[HNO_2]_{max}}{C_N - [HNO_2]_{max}}\right)^2 . \tag{17}$$

The resulting dependence is plotted in Figure 6 (nondimensionalized by C_N). As seen, the maximum fraction of HNO_2 in the mixture increases with C_N and X_H.

Note that the value of the formation energy of HNO_2 is uncertain: there is a significant discrepancy between the values from NIST and CRC, resulting in very different values of the equilibrium constant of eq. (15) ($K_{HNO2/NO/NO2}$ = 650 vs 16 mM, respectively). Here, we use value of $K_{HNO2/NO/NO2}$ =16 mM, corresponding to the CRC formation Gibbs energies, as it predicts a worse case. The difference is illustrated in S2.
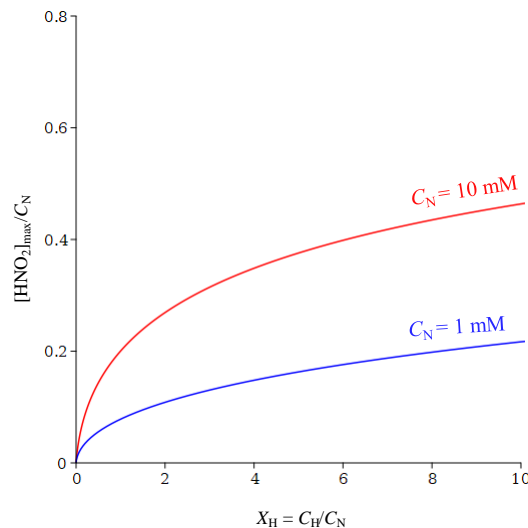

Figure 6. Maximum concentration of HNO_2 in the mixture as a function of X_H for two elemental concentrations of N, according to eq. (17). This maximum appears at $C_O = \frac{3}{2} \times C_N + \frac{1}{2} \times C_H$.

15

Nitric acid also shows some tendency for decomposition in the gaseous phase: the reaction $NO_2 + \frac{1}{2}H_2O + \frac{1}{4}O_2 \rightleftharpoons HNO_3$ in Table 3 has an equilibrium constant with the value $K_{NO2/HNO3} = 4.3$ mM$^{-3/4}$. This is small enough to result in some 40% of the acid decomposing when the mixture is close to stoichiometric and C_N is relatively small (e.g., 1-2 mM). Higher C_N and some excess of H_2O or O_2 favour HNO_3. Furthermore, solvent effects and nonideality can stabilize either the acid or NO_2 and H_2O (all Aspen models we tested predict less stable HNO_3, but they may not be suitable in this concentration region). We assume HNO_3 remains intact, again as the worst-case scenario.

Mixture of sulfur and nitrogen species. When the impurities in the stream contain both S and N, four species dominate the composition under most conditions. Furthermore, to make this 4-species map for a mixture that simultaneously contains N and S, we need a 3D diagram, as there is one additional variable compared to the previous cases: the ratio N:S. For the purpose of illustration, we consider a cross-section at a fixed value of this ratio. Figure 7 shows the 4-species diagram for $X_N = C_N/C_S = 1$. The formulae for the boundaries of each region are listed in S3 for any X_N.

As with the nitrogen 3-species diagram, there is a zone where the equilibrium reaction $NO + NO_2 + H_2O \rightleftharpoons 2HNO_2$ allows for more species than usual – namely, five (a mixture of NO, NO_2, H_2O, and HNO_2 can coexist with H_2SO_4).
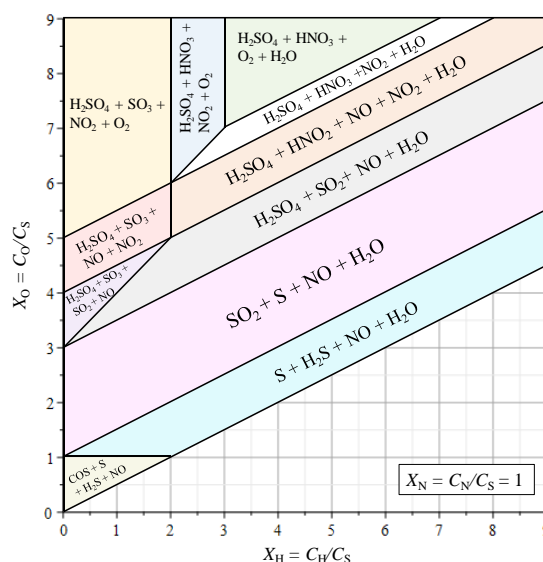
Figure 7. Combined 4-species diagram for $C_S:C_N = 1$.

2.3 Medium effects

The Gibbs reaction energies we used to calculate the stability diagrams (Figure 1-Figure 3) are for ideal gases. In the pipeline, the reactions in question are happening in a pressurized CO_2 stream instead. The presence of the solvent CO_2 is altering all K values: the medium tends to stabilize the polar species more than the nonpolar ones.

It appears that this solvent effect does not alter significantly, if at all, the composition diagrams in Figure 4-Figure 7. This is because the composition diagrams depend only on the topology of the stability map, but not the quantitative location of the equistability lines in Figure 1-Figure 3. Only if the equistability line is shifted beyond the position of a cross-section point, or towards values of lgH_2O and lgO_2 above ~0, will there be a consequence. For example, if the

16

stabilization of HNO_3 by the CO_2 medium were so large that the intercept $-4lgK_{NO2/HNO3}$ of the NO_2/HNO_3 line in Figure 2 was decreased by 6-7 units, then the shift would be beyond the cross-section between NO/NO_2 and NO_2/HNO_2. If that were the case, NO_2 and HNO_2 would not coexist in supercritical CO_2 like they can in the gas phase but would rather react: $NO_2 + HNO_2 \rightarrow NO + HNO_3$. Moreover, if the solvent effect brought two-cross section points $NO/NO_2/HNO_2$ and $NO_2/HNO_2/HNO_3$ close enough to each other, four significant components would be able to coexist (a $\{HNO_3, HNO_2, NO_2, NO\}$ region), similar to the 4-species $\{HNO_2, NO_2, NO, H_2O\}$ region discussed above. However, we have not detected such situations. It is actually more likely that HNO_3 is stabilized less than H_2O and NO_2, and the value of $K_{NO2/HNO3}$ decreases in CO_2 ($NO_2 + \frac{1}{2}H_2O + \frac{1}{4}O_2 \rightleftharpoons HNO_3$ shifts to the left), resulting in a merging of three regions to a 5-species zone $\{H_2SO_4, HNO_3, NO_2, O_2, H_2O\}$.

To illustrate the analysis, let us consider the solvent effect on the equilibrium process:

$$SO_2 + \frac{1}{2}O_2 \rightleftharpoons SO_3.$$
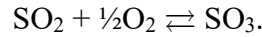
The equistability line is horizontal, $lgO_2 = -2lgK_{SO2/SO3}$, and in the supercritical CO_2 phase is related to the Gibbs energy of the reaction and the respective standard chemical potentials as follows:

$$-kT \ln K_{SO_2/SO_3}^{L} = \Delta G_{SO_2/SO_3}^{L\ominus} = \mu_{SO_3}^{L\ominus} - \mu_{SO_2}^{L\ominus} - \frac{1}{2}\mu_{O_2}^{L\ominus},$$

where $\Delta G^{\ominus}$ is the standard reaction Gibbs energy (per molecule) and $\mu_i^{L\ominus}$ are the standard chemical potentials of the respective species i in the liquid, where the standard state is 1 mM. The standard potentials in the liquid are related to those in the gas as:

$$\mu_i^{L\ominus} = \mu_i^{G\ominus} + \Delta_G^L \mu_i,$$

where $\Delta_G^L \mu_i$ is the free energy of interaction of a molecule i with the medium (related to Henry's constant of i for the liquid phase). Thus, the equilibrium constant in the liquid phase is related to that in the gas phase as:

$$-kT \ln \frac{K_{SO_2/SO_3}^{L}}{K_{SO_2/SO_3}^{G}} = \Delta_G^L \mu_{SO_3} - \Delta_G^L \mu_{SO_2} - \frac{1}{2}\Delta_G^L \mu_{O_2}. \tag{18}$$

The interaction energy $\Delta_G^L \mu_i$ consists of several contributions – Van der Waals, cavity (entropic), electrostatic molecule-medium interaction and other, second-order effects:

$$\Delta_G^L \mu_i = \mu_{el,i} + \mu_{VdW,i} + \mu_{cav,i} + ...$$

The Van der Waals interaction of one SO_3 molecule with the medium is approximately the same as that of one SO_2 and half O_2 (as the number of valence electrons is kept constant) so it is approximately cancelled in eq. (18). The entropic contribution is small for solutes of similar size to CO_2 and for a solvent like CO_2 that is not associated. Therefore, the dominant term should be expected to be the electrostatic one. Moreover, SO_3 and O_2 are nonpolar and interact weakly with the medium, while SO_2 is a triangular polar molecule interacting strongly electrostatically with the medium; hence, to a first approximation, we can write:

$$kT \ln \frac{K_{SO_2/SO_3}^{L}}{K_{SO_2/SO_3}^{G}} \approx \mu_{el,SO_2}. \tag{19}$$

For the electrostatic potential we can use the Onsager-Böttcher expression, based on Onsager's spherical cavity reaction field model [28,29]:

$$\mu_{el,SO_2} = -\frac{X_p p_{SO_2,0}^2}{2(1-\alpha_p X_p)}, \quad X_{p,Onsager} = \frac{1}{2\pi\varepsilon_0 R_{cav}^3}\frac{\varepsilon-\varepsilon_0}{2\varepsilon+\varepsilon_0}. \tag{20}$$

Here, SO_2 has dipole $p_{SO2,0} = 1.60$ D and polarizability $\alpha_p/4\pi\varepsilon_0 = 3.882$ Å^3; the density of liquid SO_2 is 1461 kg/m^3, corresponding to $R_{cav} = 2.59$ Å (see the discussion in ref. [30]). The dielectric permittivity of CO_2 at 100 bar and 25 °C (where the CO_2 density is 18.55 M) is $\varepsilon = 1.50 \times \varepsilon_0$. However, since the CO_2 medium is not very polar but is strongly quadrupolar, the medium response to the dipole of SO_2 is significantly affected by the carbon dioxide's macroscopic quadrupolarizability [30-32]. In such a case, the reaction field factor X_p is dependent on the medium's quadrupolar strength [30-32]. Rather than Onsager's eq. (20), one must use:

$$ X_p = \frac{1}{2\pi\varepsilon_0 R_{cav}^3} \frac{\varepsilon - f_p\varepsilon_0}{2\varepsilon + f_p\varepsilon_0}, \quad f_p = \frac{2+8x}{2+8x+27x^2+27x^3}, \quad x = L_Q/R_{cav}. \tag{21} $$

The value of CO_2's quadrupolar length at $p = 100$ bar and $T = 25$ °C is $L_Q = 1.09$ Å [31,32] (corresponding to a cavity radius of CO_2 of 2.61 Å).

Eq. (20) gives $\mu_{el,SO2} = -1.3 \times kT$ with the quadrupolar response model for X_p, eq. (21), compared to $\mu_{el,SO2} = -0.47 \times kT$ if the medium quadrupolarizability is ignored and $X_{p,Onsager}$, eq. (20), is used. This pronounced difference highlights the importance of including the quadrupolar solvency effect when CO_2 solutions are considered. From eq. (19), we then find:

$$ K_{SO_2/SO_3}^{L} = 0.28 K_{SO_2/SO_3}^{G}, \quad \lg K_{SO_2/SO_3}^{L} = \lg K_{SO_2/SO_3}^{G} - 0.55. \tag{22} $$

Thus, K^L is about 3 times smaller than K^G, because the quadrupolar CO_2 medium stabilizes the polar reactant SO_2. This leads to a shift of the SO_2/SO_3 line (set by $\lg O_2 = -2\lg K_{SO2/SO3}$) by 2×0.55 units, i.e. the SO_2 region in Figure 1 will expand in CO_2 medium. The regions for H_2SO_4 and H_2S will be similarly expanded in supercritical CO_2.

These shifts are all quite small compared to the distances between the lines and do not affect the topology of the maps in Figure 1-Figure 3. Since the topology alone determines the composition maps, the solvent effect on the 3-component maps in Figure 4-Figure 7 is expected to be negligible. The solvent effect on the equilibrium constant is only important in three situations. The first is the 4-species region where HNO_2, NO, NO_2 and water coexist – there, the amount of HNO_2 will depend on the solvent state, as there the equilibrium condition (16) plays a role. However, as discussed above, the value of the respective constant $K_{HNO2/NO/NO2}$ is so uncertain (see S2) that it is futile to correct it for the solvent effect. The second case is the composition nearby the boundary lines of the 3-component maps, as once again the emerging species will depend on K, see eq. (14) and the formula for [H_2SO_4] in the {SO_2, S, H_2O} region in Table 5 – if the fraction of [H_2SO_4] in this region is ~1-2% without the CO_2, the solvent may change that by a factor of around two. Finally, $K_{NO2/HNO3}$ may be sufficiently decreased in CO_2 medium so that HNO_3 partially decomposes. However, the solvent effects on $NO_2 + \frac{1}{2}H_2O + \frac{1}{4}O_2 \rightleftarrows HNO_3$ are more difficult to handle due to the radical nature of NO_2, the zwitterionic nature of HNO_3, and the tendency of both towards dimerization (see next section). Therefore, we assume that HNO_3 remains intact, as a worst-case scenario.

2.4   Nonideality

The molecules of H_2SO_4 in gas and nonpolar media associate significantly (similarly to carboxylic acids [30]). In the gas phase, H_2SO_4 molecules can form dimers and trimers through double hydrogen bonds. The geometries of these clusters have been studied in the literature [33-35]. Both the dimer and the trimer are cyclic associates; the association enthalpy of the dimer is of the order of 70 kJ·mol^{-1} [36]. Because of these strong bonds, at room

temperature and concentrations of the order of 1-10 mM, the degree of self-association is close to 100%. Moreover, sulfuric acid can also form heteroassociate structures.

This nonideal behaviour affects the chemical equilibria. For example, consider the reaction between SO_3 and water:

$$SO_3 + H_2O \rightleftarrows H_2SO_4. \tag{23}$$

The equilibrium constant used to construct the equistability SO_3/H_2SO_4 line in Figure 1 assumes that H_2SO_4 is in the form of monomers. However, there is an association-dissociation equilibrium between hydrogen-bonded acid dimers and monomers:
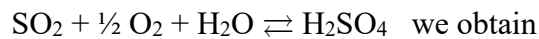
$$(H_2SO_4)_2 \rightleftarrows 2H_2SO_4, \tag{24}$$

of dimer dissociation equilibrium constant K_d. The presence of dimers modifies the mass balance of sulfur at the equistability line of SO_3 and H_2SO_4:

$$[H_2SO_4] + 2[(H_2SO_4)_2] = [SO_3] = C_S/2. \tag{25}$$

Since $[H_2SO_4] \ll 2[(H_2SO_4)_2]$ and $[H_2SO_4]^2 = K_d[(H_2SO_4)_2] = K_dC_S/4$, the equation of the equistability line that corresponds to the equilibrium (23) and the mass balance (25) reads:

$$lgH_2O = -lgK_{SO3/H2SO4} - \tfrac{1}{2}lg(C_S/K_d), \tag{26}$$

compared to $lgH_2O = -lgK_{SO3/H2SO4}$ in Table 2, in the absence of association. Similarly, for the equilibrium

$$SO_2 + \tfrac{1}{2} O_2 + H_2O \rightleftarrows H_2SO_4 \quad \text{we obtain}$$

$$lgO_2 = -2lgK_{SO2/H2SO4} - 2lgH_2O - lg(C^S/K_d), \tag{27}$$

compared to the ideal case $lgO_2 = -2lgK_{SO2/H2SO4} - 2lgH_2O$ in Table 2. Thus, the region of most stable H_2SO_4 in Figure 1 widens in all directions when self-association is taken into account.

The magnitude of this effect depends on the total concentration of sulfur and the value of the dissociation constant. In the gas phase, the dissociation constant is of the order of magnitude of $K_d^G \sim 0.001$ mM [37,38]. However, the solvent effect stabilizes the polar monomers over the non-polar dimers, and K_d^L in the liquid phase can be expected to be higher by a factor of around 50 in CO_2 [30], i.e. $K_d^L \sim 0.05$ mM. Thus, for C^S in the most relevant range, 0.5-5 mM, the term $lg(C^S/K_d)$ in eq. (26) and (27) is of the order of 1-2 units. Thus, this effect is also not strong enough to change the topology of the stability diagrams (Figure 1-Figure 3) and has little effect on the final content maps (Figure 4, Figure 5 & Figure 7), which are controlled by the mass balances rather than the values of K. The physical reason for this is that the energies to make and break chemical bonds are orders of magnitude larger than both the hydrogen bonds and the solvent effects.

Similar dimerization effects must be expected in the nitrogen stability diagram in Figure 2, further complicated by the dimerization equilibria between NO and NO_2 (to N_2O_4 and N_2O_3). Our estimates show that topology changes are again not expected. Similarly to the solvent effect, the only place where the effect is important is the regions close to the boundary lines, where the concentration of emerging species will be sensitive to the association process.

Thus, for this study, the effects from the solvent and the intermolecular association can be neglected. However, both effects are important factors for the solubility of the acids, and the approach outlined here will be used in a subsequent study to predict the changes in the solubility of acids with pressure and temperature. The solvent effect and the association processes will also affect the formation of an adsorbed film of polar species at the steel surface, which often governs the corrosion rate at undersaturated conditions [39].

3 Comparison with experimental data

The experimental data from ref. [8] are dealt with in the following manner: the initial mole fractions of the gas mixtures (containing specified amount of H_2O, SO_2, H_2S, O_2, and NO_2) are converted to elemental composition and elemental ratios X_H, X_O and X_N via eq. (8)-(9). The calculated ratios X_H, X_O and X_N are then used to identify the 3-species (or 4-species) region of the diagram into which the equilibrated composition will fall (column "region" in Table 7; the region boundaries are listed in S3). The cases without nitrogen are illustrated in the 3-species diagram of sulfur in Figure 8. The cases with ratio $X_N = 1$ are illustrated on the 4-species mixed diagram in Figure 9.

Each Pourbaix region should be expected to be associated with specific corrosion products [40], a corrosion mechanism and a respective rate of corrosion. To begin with, each region in these diagrams comes with a formula for the concentration of the acids in the gas phase (cf. Table 5, Table 6 and S3). For each experimental datum, we calculate the total acid concentration C_{acid} upon reaching equilibrium (H_2SO_4 equivalent), which we define as:

$$C_{acid} = [H_2SO_4] + \tfrac{1}{2}[HNO_3] + \tfrac{1}{2}[HNO_2]. \qquad (28)$$

The total acid concentration in the CO_2 phase is a direct measure of the corrosive potential of the mixture, loosely related to pH. The values are given in column 'C_{acid}' in Table 7 and are indicated for the cases illustrated in Figure 8-Figure 9 in brackets next to each experimental data point. The data in Table 7 is presented in order of decreasing predicted concentration of C_{acid}; hence, the most corrosive conditions are expected to be at the top of the table.
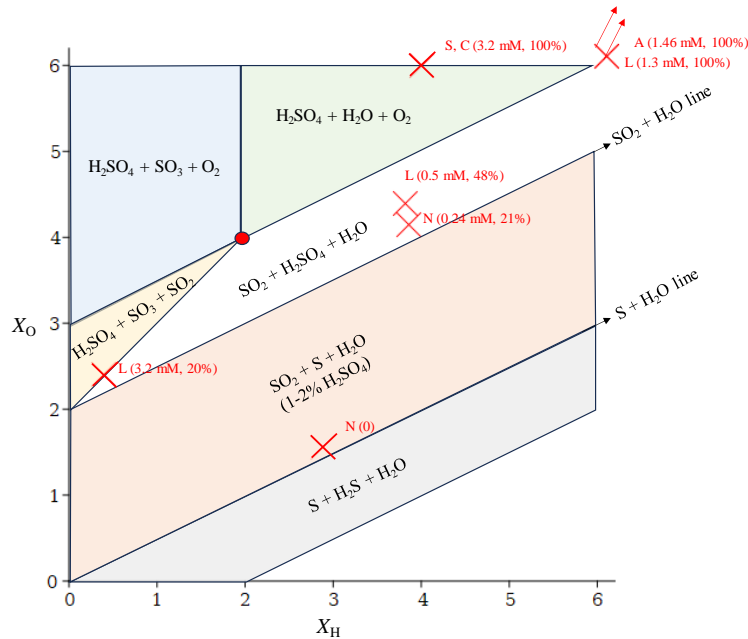
Figure 8. 3-species diagram of sulfur species (mass balance map) with experimental data from Table 7 (red crosses). The two points indicated with arrows are of very large X_O and X_H but fall in the {H_2SO_4, H_2O, O_2} region. Key: A – observed acid phase separation; S – observed sulfur phase separation; C – significant corrosion detected, L – a low corrosion rate, N – no corrosion or phase separation detected. The brackets indicate the predicted [H_2SO_4] and [H_2SO_4]/C_S.
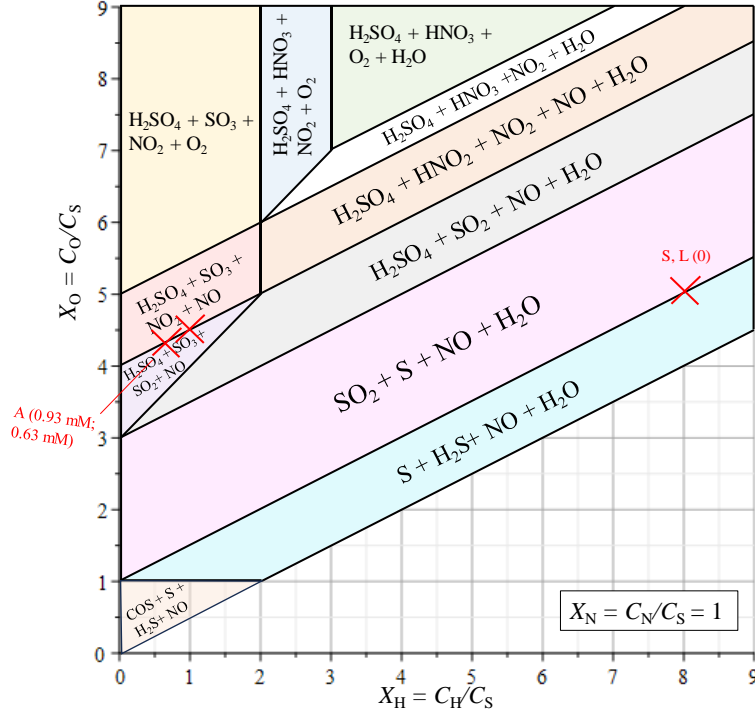
Figure 9. Combined 4-species diagram for $C_S:C_N = 1$, with data from Table 7 (red crosses). Same key as in Figure 8.

The experimental observations published in ref. [8] are listed in the last two columns of Table 7. These studies reported two phenomena taking place upon mixing: whether a new phase has separated out of the CO_2 mixture after reaction (solid sulfur or liquid acid), and what rate of corrosion has been observed for a steel coupon held in this gas mixture.

The following observations can be made:

(i) There is a very strong correlation between the value of C_{acid} calculated here and the corrosion rate and acid dropout observed in ref. [8]. When the calculated C_{acid} is > 0.5 mM (the top 15 rows of Table 7), there has been either an acid phase separating or/and an observable corrosion rate. By contrast, when the calculated C_{acid} is < 0.5 mM, significant corrosion and phase separation are not observed (except for run 22).

(ii) There appear to be only two clear exceptions, where there are discrepancies between predictions and observations. The first one is run {12}, where no corrosion appears, despite relatively high C_{acid} being predicted. Two other runs fall in the same {H_2SO_4, HNO_3, O_2, H_2O} region: {9} and {18}; one of these is quite close to the threshold C_{acid} yet the corrosion rate is below the detectable limit, and the other shows only a low rate of corrosion. Our tentative explanation for the effect is that mixed associates between H_2SO_4 and HNO_3 stabilize the solution; however, the question requires additional investigation.

The other exception is test {22}, in which acid dropout was reported, despite the equilibrium mixture appearing to be reduced (it falls in the {SO_2, S, NO, H_2O} region). A first possible explanation is an experimental artifact (e.g., the reported dropout is not of the acid phase). The second is that the reaction of the oxidizing agents NO_2 and O_2 in this mixture with SO_2 is much faster than the oxidation of H_2S, due to slow nucleation of the solid S phase (the product of oxidation of H_2S). If this is the case, there is a theoretical potential for 0.26 mM H_2SO_4 and 0.3 mM HNO_3 to form before the final equilibration to SO_2, S and NO.

The first hypothesis seems more likely as similar situations (runs {25} and {11}) follow the predicted behaviour.

(iii) Clear heterogeneous reaction kinetic effects are observed whenever H_2S is being oxidized: there is a tendency for solid sulfur to be formed even when it is not the final product corresponding to equilibrium. For example, cases {13} and {14} in Table 7 are predicted to produce significantly oxidized mixtures upon equilibration; instead, the oxidation of 100 ppm$x$ of H_2S present in the initial mixture produces sulfur, which drops out and does not react further, or at least not completely, before the end of the experiment. In the case of {13}, enough H_2SO_4 has been formed to produce a measurable corrosion rate, but for run {14}, the corrosion rate is very small, which is likely due to no water being present initially in the mixture (H_2O should eventually form through the oxidation of H_2S). Similar sulfur dropout appears whenever $[H_2S] > 60$ ppm$x$ (cases {10} and {22}), with the exception of run {8}. The kinetic differences may be due to the radical oxide NO_2, which is known to accelerate the rate of oxidation [41] – i.e. the oxidation in case {8} may be too slow in the absence of NO_2.

(iv) The only experimental datum for a mixture containing no sulfur, only nitrogen oxides, falls on the NO_2 line in Figure 5 (indicated with an arrow) and no corrosion appears at a total nitrogen concentration of $C_N = 1.14$ mM. This is, however, a very special case – even a small shift away from the NO_2 line will lead to the production of either HNO_3 or HNO_2. Actually, under similar conditions, corrosion rates were significant in some tests reported in ref. [12]. In any case, the threshold $C_{acid} > 0.5$ mM is determined for data where the acid phase is H_2SO_4-rich and not diluted by excess of water present; the presence of excess of any other polar admixtures in concentrations well above those studied in ref. [8] will certainly affect the critical value of C_{acid}.

Table 7. Comparison of predicted compositions with experimental data for CO_2 at 100 bar and 25 °C [8].

run[a]	initial impurity concentration, ppm$x$ in 18.55 M CO_2					equilibrated composition			observations	
							C_{acid} [c] [mM]	$C_{solid\ S}$ [mM]		corrosion rate [µm/year]
	H_2O	SO_2	H_2S	O_2	NO_2	region[b]			phase drop-out	
5	200	1000	–	100	–	{H_2SO_4, SO_3, SO_2}	3.71	0	none	some
13	300	100	100	350	–	{H_2SO_4, O_2, H_2O}	3.71	0	S	230
3	3000	90	–	210	–	{H_2SO_4, O_2, H_2O}	1.67	0	acid	0
7	160	80	–	–	100	{H_2SO_4, HNO_2, NO_2, NO, H_2O}	1.58	0	acid	0
19	120	38	41	95	26	{H_2SO_4, HNO_2, NO_2, NO, H_2O}	1.50	0	acid	0
14	–	100	100	140	100	{H_2SO_4, SO_2, NO, H_2O}	1.48	0	S	< 10
4	1900	80	–	240	–	{H_2SO_4, O_2, H_2O}	1.48	0	none	some
10	10	35	65	140	48	{H_2SO_4, SO_3, NO_2, NO}	1.39	0	acid + S	10
9	130	40	–	160	48	{H_2SO_4, HNO_3, O_2, H_2O}[d]	1.19	0	none	20
21	90	20	36	70	32	{H_2SO_4, HNO_2, NO_2, NO, H_2O}	1.07	0	acid	0
23	20	32	36	90	31	{H_2SO_4, SO_3, NO_2, O_2}	1.04	0	acid	0
12	50	35	–	80	30	{H_2SO_4, HNO_3, O_2, H_2O}[d]	0.93	0	none	0
15	50	100	–	–	100	{H_2SO_4, SO_3, SO_2, NO}	0.93	0	acid	0
16	34	100	–	–	100	{H_2SO_4, SO_3, SO_2, NO}	0.63	0	acid	0
20	90	30	36	70	–	{H_2SO_4, SO_2, H_2O}	0.59	0	none	some
18	35	12	10	31	10	{H_2SO_4, HNO_3, O_2, H_2O}[d]	0.50	0	none	0
6	100	35	35	60	–	{H_2SO_4, SO_2, H_2O}	0.28	0	none	0
17	100	5	6	12	5	{H_2SO_4, NO, H_2O}	0.2	0	none	0
24 [e]	250	–	–	–	70	{NO_2, H_2O}	~0.06 [e]	0	none	0
8	300	100	350	100	–	{S, H_2S, H_2O}	<0.05	7.88	none	0
11	300	–	100	–	100	{S, NO, H_2O}	<0.05	1.86	S	< 10
22	28	14	25	23	16	{SO_2, S, NO, H_2O}	<0.05	0.12	acid	0
25	200	20	20	20	10	{SO_2, S, NO, H_2O}	<0.05	0.09	none	0

[a] The run number from ref. [8] is kept for easier referencing. [b] The region is identified by calculating the elemental ratios from the initial composition and comparing with the 3-species map and the region boundaries listed in S3. [c] Acid concentration in the CO_2 phase are found using the formulae in Table 5, Table 6 and S3. Green: safe zone, C_{acid} < 0.5 mM. [d] A fraction of HNO_3 will decompose to NO_2; this will decrease C_{acid} (estimated C_{acid} – 1.06, 0.76, and 0.44 mM for runs {9}, {12}, and {18}, respectively). [e] [HNO_3] = 0.08 mM and [HNO_2] = 0.04 mM from two equilibrium conditions.

4 Discussion and conclusions

The comparison of the experimental acid formation events in Table 7 and the predicted acid equivalent concentration $C_{acid} \equiv [H_2SO_4] + \frac{1}{2}[HNO_3] + \frac{1}{2}[HNO_2]$ confirms that a high equilibrium acid content in the mixture is a key condition for corrosion to occur. We conclude that C_{acid} is a reliable indicator for prediction of acid dropout and/or unacceptable corrosion rate, correlating strongly with the experimental findings from ref. [8]. The data in Table 7 shows that, for the evaluated conditions (25 °C and 100 bar), equilibrium acid levels of $C_{acid} < 0.5$ mM are 'safe', while $C_{acid} > 0.9$ mM is a near-guarantee for observable corrosion rate or acid phase dropout. This conclusion is subject to limitations: $C_{acid} < 0.5$ mM will be safe only if the acid phase is predominantly made of sulfuric acid.

The acid that phase separates from the carbon dioxide stream is, in general, a mixture of polar components. The main component of the polar phase is nearly always going to be H_2SO_4, containing significant fraction of the polar oxidized impurities HNO_x, H_2O, NO_x, and SO_2, depending on the region. These admixtures can significantly alter the value of $[H_2SO_4]_{cr}$; e.g., in the presence of excess of water, the activity of H_2SO_4 in the polar phase decreases due to dilution, but simultaneously, the activity of the acid dissolved in the CO_2 phase decreases, due to formation of associates (see sec. 2.4 above and ref. [30]). The available data indicates that H_2O stabilizes more H_2SO_4 in the polar phase than H_2SO_4 in the carbon dioxide, but it appears that heteroassociation with HNO_3 in the nonpolar phase may be increasing $[H_2SO_4]_{cr}$, stretching the limit of the no-dropout zone. However, these effects require confirmation and will be a subject of a subsequent study.

Kinetics is another important factor that has to be considered separately. The clearest case we find is the incomplete oxidation of H_2S to solid sulfur in a number of runs in Table 7, with limited further oxidation of S. Another important question is whether radical chain initiation is possible. All oxidation-reduction reactions can be initiated by NO_2 [41], although the combination of H_2S and O_2 may also be sufficient [24]. In the absence of a radical chain initiator or a heterogeneous catalyst, the oxidation process can be arrested.

This study identifies directions for future experimentation. Eleven different zones of the 4-species diagram, Figure 7, are predicted to exist in the mixtures considered. Each zone has its own features, possibly a specific corrosion mechanism and possible dropout of a new phase (and this excludes any NH_3 present in the initial mixture). Data for only seven zones have been reported, and many data fall on the boundary lines between the regions (e.g., all of the points in Figure 9; runs {11}, {17}, {24} in Table 7 etc.), due to the design of the experiments. The zones near the boundary lines, like the $SO_2 + H_2O$ line in Figure 4, are predicted to have unique properties that set them apart from the more probable 'bulk region' cases – real-world pipeline conditions are unlikely to produce the perfect-stoichiometry mixtures that would fall on a line in the 4-species diagram. Thus, simple mixtures studied widely in the literature [8,44] may not be representative of actual pipeline corrosion, with important consequences for the design of standardized corrosion tests [13].

The work reported here can be extended without difficulties to other temperatures and pressures (see S1), to mixtures containing other N- and S-species and, thereafter, to simulations of mixing and pressurization/depressurization scenarios.

Identification of safe impurity limits is crucial for all CCS projects. CO_2 transporting carbon steel pipelines and ships are a pivotal part of the infrastructure of the CCS industry that is currently being developed, and these largely dictate the specifications for the carbon capture separation methods at the point sources. A critical range of impurities (H_2O, SO_x, H_2S, O_2, and NO_x) participate in chemical reactions upon mixing in the pipelines and produce acids that cause extreme corrosion or form precipitating sulfur. With the vast range of possible mixing scenarios in a pipeline serving many point producers of CO_2, it is difficult to eliminate the possibility of corrosion without reducing the impurity level specifications well below those typical for a single process (see Table 1). Therefore, indicators for the prediction of acid dropout and corrosion rate such as C_{acid} proposed here are of high value. The approach outlined in this paper predicts and visualizes the final reaction products with their consequential corrosion phenomena in a Poubaix-type approach. The method allows one to identify whether a mixing scenario will result in:

(i) no formation of acids, corrosion due to water and CO_2 alone (which is relatively well understood [42,43]);

(ii) formation of H_2SO_4 only, which, depending on concentration, is associated with medium to low (<20 $\mu m \cdot y^{-1}$) corrosion rate [45-47,8];

(iii) formation of a mixture of H_2SO_4 and HNO_x, or HNO_3 + HNO_2, with potential for extreme corrosion rates at the point of contact between the phase-separated polar phase and the steel (reported values > 500 $mm \cdot y^{-1}$ [48,8]);

(iv) formation of sulfur with danger of deposition at critical components of the equipment, like sensors and valves, and direct corrosion with formation of FeS [40].

In this way, a mix of impurities can be classified and the associated risk can be identified. In general, the method can be extended to precipitation of salts due to the presence of NH_3 and other basic impurities.

Finally, the work presented here indicates possible approaches to reduce the possibility of corrosion: by using small amounts of a reactive reductor or a dehydration agent, the composition of the mixture can be brought to a safe zone. For example, trace amines originating from the amine scrubbing process (ethanolamine, alkylamines) are of interest, since they may play several protective roles. In a well-formulated mixture, they may bind acids without precipitation (via acid-base reaction or heteroassociation), they may slow down radical chain reactions (by forming relatively stable radicals or by binding NO_2), and they may act as a reductor, bringing the mixture out of the acid precipitation zone. As for dehydration, it is important to keep in mind that some of the reactions in the pipeline may produce sufficient amounts of water from H_2S, and also that even a completely dehydrated CO_2 stream will eventually come in contact with water during the injection stage.

Data availability statement: all raw data used are previously published.

References

The publication contains supplementary materials:
S1. Calculation of the equilibrium constants
S2. Uncertainty in the predicted HNO_2 levels
S3. Boundaries of the regions in the mixed four-species diagram

1. International Energy Agency. World Energy Outlook 2021 (link).

2. L.O. Nord, O. Bolland, Carbon dioxide emission management in power generation, John Wiley & Sons, 2020, ch. 2.

3. B. Metz, O. Davidson, H.C. De Coninck, M. Loos, L. Meyer, IPCC special report on carbon dioxide capture and storage, Cambridge: Cambridge University Press, 2005 (link).

4. M. Mercedes Maroto-Valer, Developments and innovation in carbon dioxide capture and storage technology. Vol. 1. CRC, 2010, ch. 4, 12 etc.

5. J. Sonke, W.M. Bos, S.J. Paterson, Materials challenges with CO_2 transport and injection for carbon capture and storage, Int. J. Greenh. Gas Control. 114 (2022) 103601, https://doi.org/10.1016/j.ijggc.2022.103601.

6. J. Sonke, Y. Zheng, CO_2 Transport and injection, effect of impurities, understanding of reactions and consequences, in: AMPP Corros., AMPP, 2023 paper no. 18756.

7. AMPP Guide 21532, Guideline for Materials Selection for CO_2 transport and injection, 2023, (link).

8. J. Sonke, B.H. Morland, G. Moulie, M.S. Franke, Corrosion and chemical reactions in impure CO_2, Int. J. Greenh. Gas Control. 133 (2024) 104075, https://doi.org/10.1016/j.ijggc.2024.104075.

9. R. Barker, Y. Hua, A. Neville, Internal corrosion of carbon steel pipelines for dense-phase CO_2 transport in carbon capture and storage (CCS)–a review, Int. Mater. Rev. 62 (2017) 1–31, https://doi.org/10.1080/09506608.2016.1176306.

10. CO_2 specificaties voor Aramis transport infrastructure (link), accessed March 2024.

11. Liquid CO_2 (LCO_2) quality specifications, Northern Lights, 2024 (link), accessed March 2024.

12. B.H. Morland, A. Dugstad, G. Svenningsen, Experimental based CO_2 transport specification ensuring material integrity, Int. J. Greenh. Gas Control. 119 (2022) 103697, https://doi.org/10.1016/j.ijggc.2022.103697.

13. S.K. Kairy, S. Zhou, A. Turnbull, G. Hinds, Corrosion of pipeline steel in dense phase CO_2 containing impurities: a critical review of test methodologies, Corrosion Sci. 214 (2023) 110986, https://doi.org/10.1016/j.corsci.2023.110986.

14. R.T.J. Porter, M. Fairweather, M. Pourkashanian, R.M. Woolley, The range and level of impurities in CO_2 streams from different carbon capture sources, Int. J. Greenh. Gas Control. 36 (2015) 161–174, https://doi.org/10.1016/j.ijggc.2015.02.016.

15. I.E.A. GHG, Impact of impurities on CO_2 capture, transport and storage, Cheltenham Int. Energy Agency Greenh. Gas R&D Program. (2004).

16. A. Oosterkamp and J. Rasmen, "State of the art overview of CO_2 pipeline transport with relevance to offshore pipelines," in ASME Pipeline Engineering Symposium ETCE, Dallas, Texas, 2008.

17. M. Woods, M. Matuszewski, Quality guideline for energy system studies: CO_2 impurity design parameters, National Energy Technology Laboratory (NETL), Pittsburgh, PA, Morgantown, US Department of Energy, 2013, https://doi.org/10.2172/1556902

18. M. Pourbaix, Z. Heming, Y. XiZhen, Atlas of chemical and electrochemical equilibria in the presence of a gaseous phase. NACE, 1996.

19. M. Pourbaix, Atlas of electrochemical equilibria in aqueous solutions, NACE, 1966.

20. D.J. Young, High temperature oxidation and corrosion of metals, Elsevier, 2008, p. 36 and 368.

21. D.R. Lide, ed. CRC handbook of chemistry and physics, CRC press, 2004.

22. NIST database (link).

23. Data from Aspen Plus®, V11, Aspen Technology.

24. C.H. Bamford, C.F.H. Tipper, R.G. Compton, Reactions of non-metallic inorganic compounds, Elsevier, 1972.

25. R. Lesclaux, P. Van Khe, P. Dezauzier, J.C. Soulignac, Flash photolysis studies of the reaction of NH_2 radicals with NO, Chem. Phys. Lett. 35 (1975) 493–497, https://doi.org/10.1016/0009-2614(75)85650-8

26. J.A. Miller, M. Branch, R.J. Kee, A chemical kinetic model for the selective reduction of nitric oxide by ammonia, Combust. Flame. 43 (1981) 81–98, https://doi.org/10.1016/0010-2180(81)90008-0.

27. P. Glarborg, K. Dam-Johansen, J.A. Miller, The reaction of ammonia with nitrogen dioxide in a flow reactor: Implications for the $NH_2 + NO_2$ reaction, Int. J. Chem. Kinet. 27 (1995) 1207–1220, https://doi.org/10.1002/kin.550271207.

28. L. Onsager, Electric moments of molecules in liquids, J. Am. Chem. Soc. 58 (1936) 1486–1493, https://doi.org/10.1021/ja01299a050.

29. C.J.F. Böttcher, O.C. van Belle, P. Bordewijk, A. Rip, D.D. Yue, Theory of electric polarization, J. Electrochem. Soc. 121 (1974) 211Ca, https://doi.org/10.1149/1.2402382.

30. L.J. Farren, N. Sharifi, S.M. Clarke, R.I. Slavchov, Effect of the solvent quadrupolarizability on the strength of the hydrogen bond: Theory vs data for the Gibbs energy and enthalpy of homo- and heteroassociation between carboxylic acids and water J. Chem. Phys. 158, (2023) 214503, https://doi.org/10.1063/5.0137052.

31. I.M. Dimitrova, R.I. Slavchov, T. Ivanov, S. Mosbach, A spherical cavity model for quadrupolar dielectrics, J. Chem. Phys. 144 (2016), https://doi.org/10.1063/1.4943196.

32. I.M. Dimitrova, R.I. Slavchov, T. Ivanov, S. Mosbach, Comment on "A spherical cavity model for quadrupolar dielectrics" [J. Chem. Phys. 144, 114502 (2016)]. J. Chem. Phys. 146 (2017), https://doi.org/10.1063/1.4979717.

33. Y. Li, H. Zhang, Q. Zhang, Y. Xu, A.B. Nadykto, Interactions of sulfuric acid with common atmospheric bases and organic acids: Thermodynamics and implications to new particle formation, J. Environ. Sci. 95 (2020) 130–140, https://doi.org/10.1016/j.jes.2020.03.033.

34. L.A. Kurfman, T.T. Odbadrakh, G.C. Shields, Calculating reliable Gibbs free energies for formation of gas-phase clusters that are critical for atmospheric chemistry:(H_2SO_4) 3, J. Phys. Chem. A. 125 (2021) 3169–3176, https://doi.org/10.1021/acs.jpca.1c00872.

35. A. Givan, L.A. Larsen, A. Loewenschuss, C.J. Nielsen, Infrared matrix isolation study of H_2SO_4 and its complexes with H_2O, J. Chem. Soc. Faraday Trans. 94 (1998) 827–835, https://doi.org/10.1039/A706675I.

36. V. Kazansky, V. Solkan, Proton solvation and self-dissociation of 100% sulfuric acid: The quantum-chemical analysis, Phys. Chem. Chem. Phys. 5 (2003) 31–35, https://doi.org/10.1039/B209415K.

37. A. Kürten, S. Münch, L. Rondo, F. Bianchi, J. Duplissy, T. Jokinen, H. Junninen, N. Sarnela, S. Schobesberger, M. Simon, Thermodynamics of the formation of sulfuric acid dimers in the binary (H_2SO_4–H_2O) and ternary (H_2SO_4–H_2O–NH_3) system, Atmos. Chem. Phys. 15 (2015) 10701–10721, https://doi.org/10.5194/acp-15-10701-2015.

38. D. R. Hanson and E. R. Lovejoy, Measurement of the thermodynamics of the hydrated dimer and trimer of sulfuric acid, J. Phys. Chem. A 110 (2006), 9525–9528, https://doi.org/10.1021/jp062844w.

39. E. McCafferty. Introduction to Corrosion Science. Springer, 2010, p. 12.

40. C. Sun, J. Sun, Y. Wang, X. Lin, X. Li, X. Cheng, H. Liu. Synergistic effect of O_2, H_2S and SO_2 impurities on the corrosion behavior of X65 steel in water-saturated supercritical CO_2 systems. Corrosion Sci. 107 (2016) 193-203. http://dx.doi.org/10.1016/j.corsci.2016.02.032.

41. R.I. Slavchov, M. Salamanca, D. Russo, I. Salama, S. Mosbach, S.M. Clarke, M. Kraft, A.A. Lapkin, S. V Filip, The role of NO_2 and NO in the mechanism of hydrocarbon degradation leading to carbonaceous deposits in engines, Fuel 267 (2020) 117218, https://doi.org/10.1016/j.fuel.2020.117218.

42. J. Sonke, W.M. Bos, S. Paterson, Materials challenges with CO_2 transport and injection for carbon capture and storage, International Journal of Greenhouse Gas Control, 114 (2022) 103601, https://doi.org/10.1016/j.ijggc.2022.103601.

43. M. Cabrini, S. Lorenzi, T. Pastore, M. Radaelli. Corrosion of high CO_2 pressure pipeline steel for carbon capture transport and storage. Metallurgia Italiana, n. 6 (2014) 21.

44. K. Patchigolla, J. E. Oakey, E. J. Anthony. Understanding dense phase CO2 corrosion problems. Energy Proc. 63 (2014) 2493-2499. doi: 10.1016/j.egypro.2014.11.272.

45. M.G. Fontana, Corrosion Engineering, 3rd edition Mc Graw-Hill Book Company 1986, p. 319.

46. SP0294, NACE. Design, fabrication, and inspection of storage tank systems for concentrated fresh and process sulfuric acid and oleum at ambient temperatures. Houston, TX: NACE, 2006.

47. Z. Panossian, N.L. de Almeida, R.M. Ferreira de Sousa, G. de Souza Pimenta, L. Bordalo, A. Marques, Corrosion by concentrated sulfuric acid in carbon steel pipes and tanks – State of the art, Rio Pipeline September 2009 ref. IBP1218_09f.

48. M. Bonis, Managing the corrosion impact of dense phase CO_2 injection for an EOR purpose, in: Abu Dhabi Int. Pet. Exhib. Conf., 11-14 November 2012: p. SPE-161207, https://doi.org/10.2118/161207-MS.

Corrosion maps: stability and composition diagrams for corrosion problems in CO₂ transport

(Supplementary Information)

Radomir I. Slavchov[*,1], Muhammad Hamza Iqbal[1,2], Saeid Faraji[1], David Madden[3], Johannes Sonke[4], Stuart M. Clarke[3]

[1]School of Engineering and Materials Science, Queen Mary University of London, Mile End Road, London E1 4NS, United Kingdom
[2]Department of Mechanical Engineering, University College London, London WC1E 7JE, UK
[3]Department of Chemistry and The Institute for Environment and Energy Flows, University of Cambridge, Lensfield Road, Cambridge, CB2 1EW
[4]Shell Global Solutions International B.V.

S1. Calculation of the equilibrium constants

The equilibrium constant of a gas-phase reaction can be calculated at any temperature from thermochemical data using the Kirchhoff equation:

$$K_r = K_r^{\circ} \left(\frac{T}{T^{\circ}} \right)^{\Delta_r c_p / R} \exp \left[-\frac{\Delta_r H^{\ominus\circ} - T^{\circ} \Delta_r c_p}{R} \left(\frac{1}{T} - \frac{1}{T^{\circ}} \right) \right], \text{ where}$$

$$K_r^{\circ} = \exp\left(-\Delta_r G^{\ominus\circ} / RT^{\circ} \right). \tag{29}$$

Here the standard reaction thermodynamic quantities $\Delta_r X$ are calculated from Hess's law using formation heats, Gibbs energies and heat capacities from ref. [21,22,23]; $\circ$ indicates room temperature and $\ominus$ indicates standard state.

Table S 1. Values of the formation Gibbs energies for all relevant species.

Components	$\Delta_f G^{\circ}$ [kJ/mol], st. state 1 bar, room temperature		
	CRC [21]	NIST [22]	Aspen [23]
$H_2O(g)$	-228.6	-228.6	
$NH_3(g)$	-16.4	-16.4	
$N_2O(g)$	103.7	104.2	
$NO(g)$	87.6	86.6	
$NO_2(g)$	51.3	51.3	
$HNO_2(g)$	-46.0	-41.9	
$HNO_3(g)$	-73.5	-73.9	
$H_2S(g)$	-33.4	-33.3	
$SO(g)$	-19.9	-21.0	-21.0
$SO_2(g)$	-300.1	-300.1	
$SO_3(g)$	-371.1	-371.0	

$H_2SO_4(g)$		-653.4	
$CO(g)$	-137.2	-137.2	
$CO_2(g)$	-394.4	-394.4	
$CO(NH_2)_2(g)$		-152.56	
$CO(NH_2)_2(s)$		-197.37	
$NH_2CHO(g)$		-140.81	

The standard state used in ref. [21,22,23] is 1 bar or 1 atm; for our purposes, mM-based constants are more suitable. Therefore, K for standard state 1 bar is converted to mM-based by using the formula:

$$K[mM^\nu] = K[bar^\nu] \times (p^\ominus/RT)^\nu, \tag{30}$$

where ν is the gas mole change per mole of reaction, $\nu = \Sigma\nu_i$ (excluding all solid-state reactants), and ν_i is the stoichiometric coefficient of species i in the stoichiometric reaction.

Table S 2. Values of the equilibrium constants at room temperature.

short	reaction	lg$K$ (mM based)	
		CRC	NIST
H_2S/S	$H_2S + \frac{1}{2}O_2 \rightleftarrows S(s) + H_2O$	33.40	33.41
S/SO_2	$S(s) + O_2 \rightleftarrows SO_2$	52.58	52.58
SO_2/SO_3	$SO_2 + \frac{1}{2}O_2 \rightleftarrows SO_3$	11.64	11.62
SO_3/H_2SO_4	$SO_3 + H_2O \rightleftarrows H_2SO_4$		7.81
H_2S/H_2SO_4	$H_2S + 2O_2 \rightleftarrows H_2SO_4$		105.42
S/H_2SO_4	$S(s) + H_2O + 3/2 O_2 \rightleftarrows H_2SO_4$		72.01
SO_2/H_2SO_4	$SO_2 + H_2O + \frac{1}{2}O_2 \rightleftarrows H_2SO_4$		19.43
NO/NO_2	$NO + \frac{1}{2}O_2 \rightleftarrows NO_2$	5.56	5.39
HNO_2/HNO_3	$HNO_2 + \frac{1}{2}O_2 \rightleftarrows HNO_3$	4.02	4.81
NO/HNO_2	$NO + \frac{1}{2}H_2O + \frac{1}{4}O_2 \rightleftarrows HNO_2$	2.18	1.28
NO_2/HNO_2	$NO_2 + \frac{1}{2}H_2O \rightleftarrows HNO_2 + \frac{1}{4}O_2$	-3.38	-4.11
NO_2/HNO_3	$NO_2 + \frac{1}{2}H_2O + \frac{1}{4}O_2 \rightleftarrows HNO_3$	0.64	0.71
CO/CO_2	$CO + \frac{1}{2} O_2 \rightleftarrows CO_2$	44.26	44.26
NH_3/NO	$NH_3 + 5/4 O_2 \rightleftarrows NO + 3/2 H_2O$	42.26	42.44
$NO/NO_2/HNO_2$	$NO + NO_2 + H_2O \rightleftarrows 2HNO_2$	-1.20	-2.83
NH_3/NH_4HCO_3	$NH_3 + CO_2 + H_2O \rightleftarrows NH_4HCO_3$	-0.175	-0.173
CO_2/COS	$CO_2 + H_2S \rightleftarrows COS + H_2O$	-5.256	-5.240

All reactants but S and NH_4HCO_3 are in the gaseous phase.

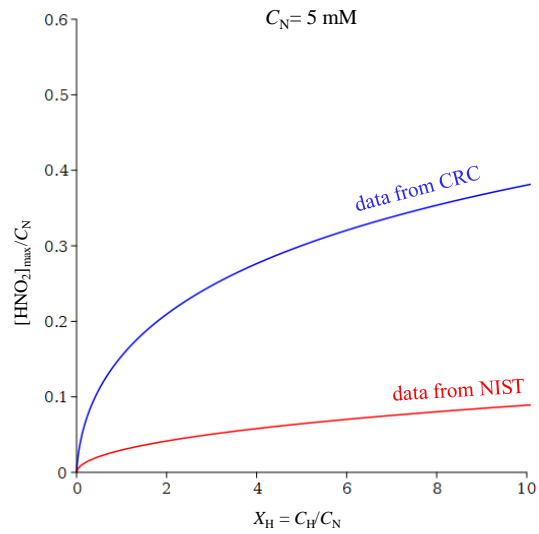# S2. Uncertainty in the predicted HNO$_2$ levels

Figure S 1. Maximum concentration of HNO$_2$ in the mixture as a function of X_H according to eq. (17) for two values of the equilibrium constant $K_{HNO2/NO/NO2}$, based on thermochemical data from two different databases [21,22].

S3. Boundaries of the regions in the mixed four-species diagram

Table S 3. Boundaries of the 4-species regions and concentration of the acids.

dominating species	boundaries	acid concentrations
$\{H_2SO_4, HNO_3, H_2O, O_2\}$	$X_H = X_N + 2$ $X_O = \frac{1}{2}X_H + 5/2X_N + 3$	$[H_2SO_4] = C_S$ $[HNO_3] = C_N$
$\{H_2SO_4, HNO_3, NO_2, O_2\}$	$X_H = 2$ $X_H = X_N + 2$ $X_O = X_H + 2X_N + 2$	$[H_2SO_4] = C_S$ $[HNO_3] = C_H - 2C_S$
$\{H_2SO_4, SO_3, NO_2, O_2\}$	$X_H = 2$ $X_O = \frac{1}{2}X_H + 2X_N + 3$	$[H_2SO_4] = \frac{1}{2}C_H$
$\{H_2SO_4, SO_3, NO_2, NO\}$	$X_H = 2$ $X_O = \frac{1}{2}X_H + 2X_{N+} 3$ $X_O = \frac{1}{2}X_H + X_N + 3$	$[H_2SO_4] = \frac{1}{2}C_H$
$\{H_2SO_4, SO_3, SO_2, NO\}$	$X_O = \frac{1}{2}X_H + X_N + 3$ $X_O = X_H + X_N + 2$	$[H_2SO_4] = \frac{1}{2}C_H$
$\{H_2SO_4, HNO_3, NO_2, H_2O\}$	$X_O = \frac{1}{2}X_H + 5/2 \times X_N + 3$ $X_O = \frac{1}{2}X_H + 2X_N + 3$ $X_O = X_H + 2X_N +2$	$[H_2SO_4] = C_S$ $[HNO_3] = -4C_N - C_H + 2C_O - 6C_S$
$\{H_2SO_4, SO_2, NO, H_2O\}$	$X_O = \frac{1}{2}X_H + X_N + 2$ $X_O = X_H + X_N + 2$ $X_O = \frac{1}{2}X_H + X_N + 3$	$[H_2SO_4] = -\frac{1}{2}C_H + C_O - C_N - 2C_S$
$\{SO_2, S, NO, H_2O\}$	$X_O = \frac{1}{2}X_H + X_N$ $X_O = \frac{1}{2}X_H + X_N + 2$	little acids
$\{S, H_2S, NO, H_2O\}$	$X_O = X_N$ $X_O = \frac{1}{2}X_H + X_N$ $X_O = \frac{1}{2}X_H + X_N - 1$	no acids
$\{COS, S, H_2S, NO\}$	$X_O = X_N$ $X_O = \frac{1}{2}X_H + X_N - 1$	no acids

{H_2SO_4, HNO_2, NO_2, NO, H_2O}	$X_H = 2$ $X_O = \frac{1}{2}X_H + 2X_N + 3$ $X_O = \frac{1}{2}X_H + X_N + 3$	$[H_2SO_4] = C_S$ $[HNO_2]$ is a solution to a cubic equation